

AEGIS: A Multi-wavelength Study of *Spitzer* Power-law Galaxies

S. Q. Park¹, P. Barmby^{2,1}, S. P. Willner¹, M. L. N. Ashby¹, G. G. Fazio¹, A. Georgakakis³,
R. J. Ivison^{4,5}, N. P. Konidaris⁶, S. Miyazaki⁷, K. Nandra⁸, D. J. Rosario⁶

ABSTRACT

This paper analyzes a sample of 489 *Spitzer*/IRAC sources in the Extended Groth Strip whose spectral energy distributions fit a red power law from 3.6 to 8.0 μm . The median for sources with known redshift is $\langle z \rangle = 1.6$. Though all or nearly all of the sample are likely to be active galactic nuclei, only 33% were detected in the EGS X-ray survey (AEGIS-X) using 200 ks *Chandra* observations. The detected sources are X-ray luminous with $L_X > 10^{43} \text{ erg s}^{-1}$ and moderately to heavily obscured with $N_H > 10^{22} \text{ cm}^{-2}$. Stacking the X-ray-undetected sample members yields a statistically significant X-ray signal, suggesting that they are on average more distant or more obscured than sources with X-ray detections. The ratio of X-ray to mid-infrared fluxes suggests that a substantial fraction of the sources undetected in X-rays are obscured at the Compton-thick level, in contrast to the X-ray-detected sources, all of which appear to be Compton-thin. For the X-ray-detected power-law sources with redshifts, an X-ray luminosity $L_X \sim 10^{44} \text{ erg s}^{-1}$ marks a transition between low-luminosity, blue sources dominated by the host galaxy to high-luminosity, red power-law sources dominated by nuclear activity. X-ray-to-optical ratios, infrared variability, and 24 μm properties of the sample are consistent with the identification of infrared power-law

¹Harvard-Smithsonian Center for Astrophysics, 60 Garden Street, Cambridge, MA 02138, USA; spark@cfa.harvard.edu

²Department of Physics & Astronomy, University of Western Ontario, London, ON N6A 3K7, Canada

³National Observatory of Athens, I. Metaxa & V. Paulou, Athens 15236, Greece

⁴UK Astronomy Technology Centre, Science and Technology Facilities Council, Royal Observatory, Blackford Hill, Edinburgh EH9 3HJ, UK

⁵Institute for Astronomy, University of Edinburgh, Blackford Hill, Edinburgh EH9 3HJ, UK

⁶UCO/Lick Observatory, University of California Santa Cruz, 1156 High Street, Santa Cruz, CA 95064

⁷National Astronomical Observatory of Japan, Osawa Mitaka Tokyo 181-8588, Japan

⁸Astrophysics Group, Imperial College London, Blackett Laboratory, Prince Consort Road, London SW7 2AZ, UK

sources as active nuclei, but a rough estimate is that only 22% of AGNs are selected by the power law criteria. Comparison of the power-law selection technique and various IRAC color criteria for identifying AGNs confirms that high-redshift samples selected via simple IRAC colors may be heavily contaminated by starlight-dominated objects.

Subject headings: galaxies: active — infrared: galaxies – X-rays: galaxies

1. INTRODUCTION

A census of active galactic nuclei (AGNs) is a necessary prerequisite for constraining the accretion history of the Universe, describing the origin of the cosmic background, and understanding galaxy formation. X-ray detection is often used as an efficient method of finding relatively uncontaminated samples of AGNs (Mushotzky 2004). Large numbers of AGNs can be found in deep X-ray surveys, where the AGN density is an order of magnitude higher than that found in deep optical observations via broad emission lines (e.g., Hall et al. 2000; Steidel et al. 2002; Bauer et al. 2004). X-ray surveys have now resolved $\sim 90\%$ of the cosmic X-ray background (CXRB) at 2–8 keV (e.g., Mushotzky et al. 2000; Bauer et al. 2004; Hickox & Markevitch 2006). However, current X-ray telescopes lose sensitivity toward higher energies. Only 60% of the X-ray background is resolved at 6–8 keV, and this fraction drops further to 50% at >8 keV (Worsley et al. 2004, 2005). Synthesis models of the hard X-ray background spectrum require larger numbers of AGNs than are currently observed. Heavily obscured, Compton-thick AGNs are expected to outnumber unobscured AGNs by a ratio of $\sim 4:1$ (e.g., Maiolino & Rieke 1995; Comastri et al. 2001; Gilli et al. 2001, 2007), though the exact value is still not well constrained. Deep observations can sometimes detect the most luminous of these hard X-ray sources (Tozzi et al. 2006; Georgantopoulos et al. 2007), but even the deepest X-ray surveys can miss large populations of obscured AGNs.

With the launch of highly sensitive infrared (IR) instruments aboard the *Spitzer Space Telescope* (Werner et al. 2004), IR surveys have become a useful complement to X-ray and visible-light AGN searches. AGNs are thought to have a dusty environment (often imagined as a torus) surrounding an optically- and X-ray-bright accretion disk centered on a massive black hole (e.g., Antonucci 1993; Urry & Padovani 1995). Incident X-rays from the central engine can be absorbed and reprocessed by the circumnuclear dust and re-emitted at longer wavelengths, making AGNs IR-bright (Barvainis 1987; Granato & Danese 1994; Nenkova et al. 2002). The infrared bands are also much less affected by dust extinction than the optical, making them ideal for identifying obscured sources.

There have been several studies of AGN selection using *Spitzer* mid-IR colors (e.g., Lacy et al. 2004; Stern et al. 2005; Hatziminaoglou et al. 2005) or other IR properties (e.g., Martínez-Sansigre et al. 2005; Donley et al. 2005; Daddi et al. 2007; Fiore et al. 2008; Park et al. 2008). One straightforward way to search for obscured AGNs is to study their spectral energy distributions (SEDs) (Alonso-Herrero et al. 2006; Barmby et al. 2006; Donley et al. 2007; Cardamone et al. 2008; Donley et al. 2008). In the mid-IR, AGNs can often be distinguished by their red power-law SEDs, which can extend from the UV all the way into the far-IR (Rees et al. 1969; Neugebauer et al. 1979; Ward et al. 1987; Elvis et al. 1994; Assef et al. 2010). This behavior is thought to arise from a combination of thermal and non-thermal components near the dusty nucleus that together produce a broad SED rather than from a single power-law emission source (Rieke & Lebofsky 1981; Barvainis 1987; Kotilainen et al. 1992; Klaas et al. 2001). Analysis of broadband SEDs therefore proves to be a powerful diagnostic, differentiating AGNs from sources dominated by starlight. The latter generally have a blue mid-IR power-law SED corresponding to the Rayleigh-Jeans tail of the blackbody spectrum or else do not fit a power law at all due to their 8 μm PAH emission or 1.6 μm stellar bump.

Finding large samples of AGNs in multiwavelength surveys requires both wide area and good sensitivity. This paper uses deep *Spitzer Space Telescope* data to select a sample of 489 red power-law sources in the Extended Groth Strip (EGS). The EGS ($\alpha = 14^{\text{h}}17^{\text{m}}$, $\delta = +52^{\circ}30'$) is a premier extragalactic survey field observable from the Northern Hemisphere that fits both criteria (Davis et al. 2007). The EGS has been surveyed at nearly every available wavelength to considerable depth and area, and it spans more than $\sim 2^{\circ}$ by $10'$ in the 9.1 ks IRAC pointings (Barmby et al. 2008). The region’s high ecliptic and Galactic latitudes make it well-suited for studying extragalactic sources with little Galactic contamination.

The unique combination of depth and size makes the EGS an ideal field for an AGN search: it is shallower but larger than the combined GOODS fields and smaller but deeper than the COSMOS field at most wavelengths. Previous IRAC power-law studies have been done in fields with much deeper X-ray exposures (~ 1 Ms) but shallower IRAC observations (~ 500 s, e.g., Donley et al. 2007). The size and depth of the EGS field in the IR bands allows us to probe different redshift regimes with larger samples and improved statistics. This study therefore provides a view of power-law sources that is complementary to previous work and extends the work of Barmby et al. (2006), who analyzed the IR properties of X-ray selected AGNs in a small portion of the EGS. Multiwavelength data are utilized to further study the properties of these AGN candidates, including deep *Chandra X-ray Observatory* pointings to confirm AGN status and control contamination.

This paper proceeds as follows: §2 introduces the data sets used, and §3 describes

the power-law AGN selection process. §4 compares the power-law selection with other IR selection methods. §5 discusses the sample redshift distribution and §6 the spectral energy distributions. §7 details the X-ray, IR, visible, and radio properties of the power law sample. A summary is given in §8. Throughout this paper, we adopt Λ CDM cosmology with $H_0 = 71 \text{ km s}^{-1} \text{ Mpc}^{-1}$, $\Omega_M = 0.27$, and $\Omega_\Lambda = 0.73$. All magnitudes are in AB units unless otherwise noted.

2. OBSERVATIONS AND DATA REDUCTION

Infrared Array Camera (IRAC; Fazio et al. 2004) observations of the EGS were obtained in 2003–2004 as part of Guaranteed Time Observation (GTO) program 8 with time contributed by G. Fazio, G. Rieke, and E. Wright. Each position was observed for approximately 9.1 ks at all four IRAC wavelengths. The data were processed by the *Spitzer* Science Center IRAC pipeline and custom software, and sources were identified using SExtractor. Barmby et al. (2008) give details of the observations and reductions and list source photometry in a variety of apertures. This paper uses the photometry in the $3''.06$ diameter aperture, for which the data yield 50% point-source completeness limits of 1.1, 1.2, 6.3, and $6.9 \mu\text{Jy}$ at 3.6, 4.5, 5.8, and $8.0 \mu\text{m}$, respectively.¹ Barmby et al. also discussed the observational uncertainties, which are used here with an additional 5% of the flux density added in quadrature to allow for systematic errors.

The IRAC data are supplemented by observations from the Far-Infrared Deep Extragalactic Legacy (FIDEL) project² taken with the Multiband Imaging Photometer (MIPS; Rieke et al. 2004) aboard *Spitzer*. The FIDEL data fully overlap the IRAC EGS pointings and include a ~ 12 ks exposure at $24 \mu\text{m}$ and a ~ 5.4 ks exposure at $70 \mu\text{m}$. Observations used here are from the preliminary FIDEL catalog (dated 2008 Aug 28 — M. Dickinson, private communication 2008). Source extractions were done with DAOPHOT, which uses PSF fitting to determine magnitudes. The $70 \mu\text{m}$ source catalog is 99% complete for flux densities above 5 mJy. The limiting flux density at $24 \mu\text{m}$ is $30 \mu\text{Jy}$ (Salim et al. 2009). For the FIDEL data, our analysis uses only the observational uncertainties calculated by DAOPHOT.

The X-ray data were obtained with eight 200 ks pointings using the ACIS-I instrument on the *Chandra X-ray Observatory* and reach a limiting flux of $5.3 \times 10^{-17} \text{ erg cm}^{-2} \text{ s}^{-1}$

¹This paper actually used a not-quite-final version of the published catalog. The only effect of this is that IRAC flux densities used here and given in Table 2 are 3% higher than the final values. This has no effect on sample selection and trivial effect on ratios of IRAC to other-wavelength fluxes.

²<http://ssc.spitzer.caltech.edu/legacy/fidelhistory.html>; PI: Mark Dickinson

(3.8×10^{-16} erg cm $^{-2}$ s $^{-1}$) in the 0.5–2 (2–10) keV band. These observations currently represent the third deepest X-ray survey in the sky, and an extra 1.8 Ms of data have been taken in *Chandra* cycle 9 to observe the central fields of the EGS to a depth of 800 ks each. The 200 ks data were reduced using the CIAO data analysis software version 3.3 as described by Laird et al. (2009). Of the 1325 sources in the existing AEGIS-X catalog, 882 are within the IRAC region. At the 200 ks X-ray depth, the majority of the detected sources should be active nuclei based on their redshifts and luminosities: of the ~ 250 cataloged sources with IRAC counterparts and reliable redshifts, 95% have luminosities $L_{2-10 \text{ keV}} > 10^{42}$ erg s $^{-1}$ as expected for AGNs, and all sources have $L_{2-10 \text{ keV}} > 10^{40}$ erg s $^{-1}$. In the EGS field, a previous study (Barmby et al. 2006) found a stellar contamination rate of $\sim 3\%$ among the X-ray identified objects.

Additional data used include visible photometry from the Suprime camera on the Subaru telescope (S. Miyazaki 2005, private communication) with a 5σ limiting AB magnitude of $R \sim 27$. Additional visible-light data were taken in the B , R , and I bands from the Canada-France-Hawaii Telescope with limiting AB magnitudes of 24.5, 24.2, and 23.5 respectively at 8σ (Coil et al. 2004) as well as in the u' and g' bands with Megacam (McLeod et al. 2006) at the MMT with 5σ limiting AB magnitudes of 26.5 and 27.2, respectively (Ashby et al. in prep.). We used near-IR observations in the J and K bands from the Wide-Field Infrared Camera on the Palomar 5-m telescope (Bundy et al. 2006) with limiting magnitudes of 23 mag (Vega) and 20.6 mag (Vega) at 5σ for J and K , respectively. All these visible and near-IR data sets span the entire IRAC field except that the J -band images cover only one third of the field. Optical morphology was studied using I (F814W) band images from the Advanced Camera for Surveys (ACS) aboard the Hubble Space Telescope (HST) (Lotz et al. 2008). We utilize the AEGIS20 radio survey (Ivison et al. 2007) which comprises 108 hr of observations with the Very Large Array in its B configuration and covers two thirds of the IRAC field with a source sensitivity limit of 50 μ Jy. Finally, we use spectroscopic redshifts obtained across two-thirds of the field by the Keck DEIMOS spectrometer as part of the DEEP2 survey (Davis et al. 2003) as well as targeted redshifts available over the whole field from 2006–2007 observations on the MMT Hectospec fiber spectrograph (Coil et al. 2009).

The final parent sample for power-law selection is restricted to sources detected in all four IRAC channels with signal-to-noise ratios of at least five. Because the X-ray data provide an important and straightforward way of confirming AGN status, the analysis is further limited to IRAC sources within the *Chandra*-observed field.³ The resulting 0.35 deg 2 survey area contains over 11,000 four-band IRAC sources as well as over 700 X-ray sources

³Restricting to the *Chandra* area eliminates only 5% of the four-band IRAC sources.

with Poisson false probabilities $< 4 \times 10^{-6}$.

The multiwavelength datasets were cross-identified by matching all sources to the IRAC catalog positions using a $1''.5$ search radius. This procedure nearly always resulted in a unique match, and in the few ambiguous cases, the source closest to the IRAC position was taken as the counterpart. Comparing this approach to the likelihood-matching method used for the X-ray data by Laird et al. (2009) results in a discrepancy of less than 1% in our final AGN candidate sample. Because *Chandra*’s point spread function (PSF) worsens with increasing off-axis angles (OAAs), in matching the IRAC sources to the X-ray catalog, we checked for sources at large OAAs where the possibility of a mismatch due to positional inaccuracies is higher. The *Chandra* pointing is wider than the IRAC field, and therefore many of the sources with the largest OAAs do not lie within the shared area. Out of 719 X-ray counterparts, only ten X-ray matches have OAAs greater than $9'$, and four of these have OAAs greater than $10'$. Therefore, we are confident of the vast majority of the IRAC-*Chandra* associations.

3. POWER-LAW SAMPLE SELECTION

In the infrared, the slope of a galaxy SED may be characterized by a power law behavior of flux density with frequency $S_\nu \propto \nu^\alpha$. AGN SEDs often follow a negative-sloping (red) power law, which may arise from either thermal or non-thermal emission originating near the central region (e.g., Rees et al. 1969; Neugebauer et al. 1979; Elvis et al. 1994). In contrast, stellar-dominated sources at low redshift generally exhibit positive (blue) IRAC power-law emission following the Rayleigh-Jeans tail of the blackbody spectrum. If $z \gtrsim 1$, the SED of stellar-dominated sources may deviate from a power law because of the $1.6 \mu\text{m}$ stellar emission bump, which arises from the minimum in the opacity of the H^- ion present in stellar atmospheres, but the overall slope is likely to be blue or at least flat unless $z \gtrsim 2$.

For this paper, we defined a sample of IR-selected AGNs by choosing sources with SEDs that follow a power law in the four IRAC bands from 3.6 to $8.0 \mu\text{m}$ (observed, not rest) wavelengths. A good fit was defined by small chi-square such that $P(\chi^2) \geq 0.1$, i.e., a source having a true power law SED has a 10% chance of being excluded from the sample by random observational errors. Galaxies fitting a power-law SED were further classified as red or blue. A limit of $\alpha \leq -0.5$ was chosen to select our final sample of AGNs following Alonso-Herrero et al. (2006), and throughout this paper, we refer to “red” power laws as those with $\alpha \leq -0.5$, while “blue” power laws refer to those with $\alpha > -0.5$. The cut-off was based on the average visible–IR spectral slope of AGNs $\alpha \sim -1$ (Elvis et al. 1994; Neugebauer et al. 1979) as well as the visible spectral indices of $\alpha = -0.5$ to -2 of QSOs from the Sloan Digital Sky Survey (SDSS; Ivezić et al. 2002). Stern et al. (2005) found a

similar slope in the IRAC bands of $\alpha = -1.07 \pm 0.53$ among broad line AGNs.

There are 489 sources within the IRAC/*Chandra* shared field that are well fit to a red power law with $\alpha_i \leq -0.5$, where α_i is the spectral index from 3.6 to 8.0 μm . (See Table 1 for a listing of fit categories and Figure 1 for a sample fit. Uncertainties in slope for individual objects range between ± 0.08 and ± 0.21 .) These sources comprise only 4% of the IRAC sources in the field. In comparison, 30% of the IRAC sources are well fit by a power law with $\alpha_i > -0.5$. Barmby et al. (2006) similarly found that 40% of IRAC sources fit a power law⁴ with 7% having $\alpha_i < 0$ and 33% having $\alpha_i > 0$. (In practice, the differing cutoff between “red” and “blue” makes little difference; see Fig. 2.) Red power-law sources and blue power-law sources have similar median flux densities at 8 μm but diverge toward shorter wavelengths. At 3.6 μm , the median flux density of the blue sample is five times higher than the median flux density of the red sample. The remaining 66% of sources do not fit a power law according to our criterion: 10% have red slopes with best-fit $\alpha_i < -0.5$ but $P(\chi^2) < 0.1$, and 55% have blue slopes but $P(\chi^2) < 0.1$. The 489 sources identified in our sample as having red power-law (PL) fits are referred to here as PL AGNs and are listed in Table 2. These sources were selected on the basis of their IRAC spectral slopes only and therefore should not be biased by X-ray or visible-light AGN-like properties. The assumption that these sources are AGNs will be justified below.

We also selected a sample of sources fitting a red power law from 3.6–24 μm , thereby doubling the baseline used to determine spectral slope. The vast majority of MIPS sources (nearly all of which were detected by IRAC) cannot be fit to a power law, red or blue. While most of the IRAC sources are generally brighter toward the blue, the MIPS sources have much redder mid-IR emission, and only 0.5% are well fit by a blue power law while 16% are blue but poorly fit by a power law. 82% of MIPS sources are red but poorly fit by a power-law, and finally 2% (168) of MIPS sources are well fit by a red power law from 3.6 to 24 μm . The predominance of red sources is expected from the lower sensitivity limit of the MIPS instrument compared to IRAC: IRAC sources detected by MIPS are likely to be red unless they have extremely bright IRAC flux densities. The 168 MIPS sources that fit a red power law are hereafter referred to as the 3.6–24 μm power law sample to distinguish them from the PL AGN sample that is the main focus of this study. All but 15 of these 168 sources are in the PL AGN sample. Of these 15, 12 are red in the IRAC bands but were excluded from the PL AGN sample because they do not fit a power law well enough at 3.6–8 μm . The other three fit a power law in the IRAC bands but a blue one with $\alpha_i \approx -0.35$ for all three sources. These three sources barely made the cutoff for a good 3.6–24 μm red power-law fit

⁴“Fit” is defined in their paper by the less stringent criterion $P(\chi^2) > 0.01$.

with $P(\chi^2) \approx 0.11$ and the 3.6 to 24 μm slope $\alpha_m \approx -0.65$.

The distributions of fitted spectral slopes are shown in Figure 2. As shown, PL AGNs make up only a small fraction of the total number of IRAC sources; their median spectral index is $\alpha_i = -1.03 \pm 0.03$. There is no significant statistical difference between this calculated median slope and the slope of the Elvis et al. (1994) median QSO SED, which is $\alpha = -1.13$ at IRAC wavelengths. Narrow-line AGNs are expected to have steeper slopes than broad-line AGNs, as their visible and near-IR emission is much more heavily obscured than their mid-IR emission, but there is no evidence of bimodality in the histogram of PL AGN slopes.

The 3.6–24 μm power law objects do appear to fall into two clear groups. The majority of them are red throughout the mid-IR with $\alpha_i \leq -0.5$; these have a median spectral index of $\alpha_i = -1.11 \pm 0.03$. There is also a small group of sources that fit a blue power law from 3.6 to 24 μm and cluster at $\alpha_i \approx 1.8$, which is the slope of sources dominated by starlight. These have colors $([3.6] - [8.0])_{\text{Vega}} \approx 0$, as expected for stars. For most sources, there is good agreement in spectral slope between sources well fit by a power law in both 3.6–8.0 μm and 3.6–24 μm (see Figure 3). The X-ray sources span a wide range of α_i but are overwhelmingly red in their 3.6–24 μm colors. These will be discussed further in §7.1.

The PL AGN with the steepest slope has $\alpha_i = -2.76 \pm 0.14$. This is consistent with the maximum steepness found by other studies and suggests a cutoff of mid-IR SED shape: Alonso-Herrero et al. (2006) found a maximally steep visible-to-IR slope of -2.8 among their power-law sources, and Donley et al. (2007) found $\alpha = -3.15$. The optically faint X-ray sources in the CDFS studied by Rigby et al. (2005) had a maximum steepness of $\alpha = -2.9$, and Stickel et al. (1996) found a limit of $\alpha \sim -2.5$ among a sample of flat-spectrum radio sources. Figure 2 shows that the PL AGNs with the steepest spectral indices never fit a power law from 3.6–24 μm . Instead the SED turns over somewhere between 8 and 24 μm , and the actual 24 μm flux densities of these sources are several times lower than predicted by a simple extension of the IRAC power law.

4. PL SELECTION AND OTHER IR TECHNIQUES

4.1. Color-Color Plots

AGNs are generally redder than normal galaxies in the infrared, and many studies have used this fact to select AGNs via their positions in color-color space. For example, Lacy et al. (2004) and Hatziminaoglou et al. (2005) defined separate AGN selections by studying luminous type 1 Sloan Digital Sky Survey QSOs in the *Spitzer* First Look Survey and the *Spitzer* Wide-Area Infrared Extragalactic Survey, respectively, and Stern et al. (2005) plotted

spectroscopically confirmed AGNs in the Boötes field to define their selection region.

Power-law selection is similar in principle to the IRAC color-color methods. Both techniques search for luminous objects where the nuclear activity outshines light from the host galaxy in the IRAC bands, which sample the SED between the stellar emission expected at visible wavelengths and the dust emission at mid-IR wavelengths. However, the power-law selection is much stricter, requiring in effect three color criteria rather than two for selection of AGN candidates. For comparison, Figure 4 shows our PL AGN sample on the color-color plots used by Lacy et al. (2004) and Stern et al. (2005). All of the PL AGNs are contained within the Lacy-defined wedge. However, the selection used by Lacy et al. is quite broad; the wedge selects 60% of the entire IRAC parent sample. The wedge also contains 80% of the X-ray sources, but the X-ray sources comprise only 8% of the total sources in the AGN region. Even if the IRAC catalog is truncated to retain only sources that exceed the flux density limits of Lacy et al., 40% of the IRAC general population is contained within the AGN region, though the X-ray detection rate goes up to $\sim 40\%$. The Stern et al. (2005) selection is less inclusive, containing just 18% of the IRAC sample but 96% of our PL AGNs. Fifty percent of the X-ray sources are contained by the wedge, and the X-ray detection rate within the wedge is 17%. The X-ray sources overall show a wide range of colors and do not appear to lie within any well-contained region of color-color space. Barmby et al. (2006) and Cardamone et al. (2008) similarly found that no IR color selection method can reliably select all AGNs while avoiding the normal galaxy population.

Though color selections detect many low-luminosity AGNs due to the broadness of the criteria, the depth of the IRAC data is important. The EGS field, with its much deeper IRAC data, probes different redshift regimes than the shallow fields studied by Lacy et al. (2004), who considered sources at $z \sim 0.3$, and by Stern et al. (2005), whose sample was mostly sensitive to galaxies at $z < 0.6$. The results of previous color-color AGN selection studies have been efficient and reliable in part because they focused on low redshift regimes. In contrast, at the higher redshifts typical of our study, many non-AGNs migrate into the AGN color selection wedge. Barmby et al. (2006) found that while AGN SED templates stay within the AGN selection wedges at all redshifts, starburst and normal galaxy templates have colors outside the AGN wedges at low redshift, but the colors migrate into the AGN wedge at high redshifts. Georgantopoulos et al. (2008), Donley et al. (2008), and Assef et al. (2010) similarly found that star-forming templates enter the selection wedges both at low and high redshifts, though they avoid the locus carved out by the power-law selection (see Figure 6 of Barmby et al. 2006 or Figure 4 of Donley et al. 2008). The templates suggest that a high degree of stellar contamination is unavoidable when the color selection technique is applied to deeper samples. Contamination can be reduced by restricting the sample to relatively high $24 \mu\text{m}$ flux densities, but Donley et al. (2008) found that even for $S_{24} > 0.5 \text{ mJy}$,

half of the color-selected sources in their sample cannot be confidently identified as AGNs. Power-law selection is a much more reliable method of finding AGNs: most of the secure AGN identifications among the color-selected galaxies in the GOODS-S field were contained in the power-law sample (Donley et al. 2008).

The expectation from templates is confirmed by the EGS IRAC data. Figure 5 shows the evolution of IRAC colors for sources with and without measured redshifts. At $z < 0.4$, the $6.2\ \mu\text{m}$ and $7.7\ \mu\text{m}$ PAH features can still dominate the $8.0\ \mu\text{m}$ -band emission, and the plot is largely populated by sources with roughly constant blue $S_{5.8}/S_{3.6}$ colors but spanning a wide range of red $S_{8.0}/S_{4.5}$ colors. These are likely to be nearby, stellar-dominated galaxies with strong aromatic emission redshifting through the $8\ \mu\text{m}$ band. At intermediate redshifts $0.4 < z < 1.4$, sources migrate closer to the AGN region of the color-color plot as the K-correction shifts objects towards the red. At $z > 1.4$, nearly every object has colors consistent with the AGN wedge. Thus, though we cannot assess starburst contamination at high redshifts due to the biases inherent in our redshift survey (see §5), we reiterate the need for caution to avoid contamination from star-forming galaxies in using IRAC color-color selection of AGNs. We also caution that the color changes with redshift seen in Figure 5 should not be interpreted as population evolution because the IRAC bands sample different rest wavelengths at each redshift.

4.2. Visible to IR Colors

Another technique for finding AGNs is to select on very red infrared-to-visible or infrared-to-UV color (e.g., Daddi et al. 2007; Dey et al. 2008; Fiore et al. 2008; Polletta et al. 2008; Pope et al. 2008). This technique has principally been applied to find X-ray-faint (possibly Compton-thick) AGNs. Adopting the approach of Fiore et al. selects 89 sources in the EGS with $S_{24}/S_R \geq 1000$, $R - K > 4.5$, and $S_{24} > 40\ \mu\text{Jy}$. Only two of these fit a red IRAC power-law. The nature of the “IR-excess” selection is to choose optically faint sources, $R > 25.5\ \text{mag}$, and as a result only one of the 89 IR-excess sources in the EGS has a spectroscopic redshift (with $z = 1.1$). Though the majority of these galaxies cannot be fit to either a red or blue power-law, $\sim 75\%$ have blueward-sloping SEDs. Dey et al. (2008) found a similar result for IR-excess galaxies, at least for $S_{24} \lesssim 0.8\ \text{mJy}$: most have SEDs containing a stellar emission component. Thus at least a major portion of the IR light in IR-excess-selected objects is likely to be starlight, even if an AGN is also present.

4.3. Contamination of the Power-law Method

Little contamination is expected from stellar-dominated sources in our PL AGN sample. Systems with infrared emission dominated by star formation and also galaxies with high levels of starlight from an older stellar population show curvature in their SEDs and thus will not enter the PL AGN sample. As shown below, the multiwavelength properties of the PL AGN sample also point to strong nuclear activity. The red IRAC colors of the PL AGNs are unlikely to arise from PAH emission in the $8\ \mu\text{m}$ band; such emission would not produce an overall power law SED. Furthermore, of the sources with redshifts (§5), only four have $z < 0.5$, and none has $z < 0.4$. For higher redshifts that characterize the bulk of the PL AGNs, the strong PAH features are outside the IRAC bands. While the PL AGNs may have stellar emission at some level — even enough to be a major component of the bolometric luminosity — it should not dominate the light observed at IRAC wavelengths.

PL AGN SEDs generally follow AGN templates with no evidence of stellar bumps, but an attempt to model the UV-MIR SEDs of the PL AGNs more precisely was inconclusive. Unfortunately, PL AGNs SEDs offer little information because of their lack of spectral features. The possibility that some objects in the PL AGN sample are really starbursts cannot be directly tested because, if they are starbursts, they must have photometric redshifts $z \geq 2$, while spectroscopic measurements at these high redshifts are limited to AGNs (§5). Modeling the UV-MIR SEDs of X-ray undetected PL AGNs is particularly difficult because most of these sources have very low or undetected visible flux densities. However, our X-ray stacking analysis (§7.1.2) demonstrates that these sources have hard X-ray emission and are likely to be obscured AGNs.

We also studied the SED templates for a luminous infrared galaxy (LIRG) and an ultraluminous infrared galaxy (ULIRG) made from average composite fits of observed LIRGs and ULIRGs (Donley et al. 2008). An IRAC power-law shape cannot be obtained simply by redshifting the (U)LIRG SED templates we tried to the maximum redshifts ($z \approx 3.5$) that we observe. Alonso-Herrero et al. (2006) suggested that cool ULIRGs at $z > 2$ and with $\alpha_i > -1$ could contaminate a power-law AGN sample, but the SED templates in their Figure 11 show curvature resulting from the $1.6\ \mu\text{m}$ stellar bump in the IRAC wavelength range. The stellar bump should exist whenever a substantial fraction of the rest $1.6\ \mu\text{m}$ light comes from evolved stars, and its absence (by definition) in our PL AGN sample should eliminate most if not all cool ULIRGs. More recently, Narayanan et al. (2010) have presented theoretical models in which reddened starlight from a young population plus an AGN component can exhibit a power law SED during brief phases of a merger. There are 21 PL AGNs with spectroscopic $z > 2$, but their visible spectra all show AGN emission lines (§5). Moreover, all but four have X-ray hard-band detections with $L_{2-10\text{keV}} > 10^{44}\ \text{erg s}^{-1}$. Members of our PL AGN class that

are too faint in visible light to have spectra could conceivably be high-redshift ULIRGs of the type proposed by Narayanan et al., but the brevity of the power-law phase suggests such contaminants should be uncommon. The multiwavelength data on the PL AGN sample also suggest little contamination. Redshifts and thus luminosities for any star-forming galaxies contaminating the PL AGN sample would have to be very high.

5. REDSHIFT DISTRIBUTION AND EVOLUTION

Because the power-law selection tends to choose sources that are optically faint (§7.3), the PL AGN sample has a smaller rate of redshift measurement than the general IRAC sample. This is true despite the fact that many of the Hectospec redshifts (Coil et al. 2009) specifically targeted red power-law sources, X-ray sources, and radio galaxies. Only 13% of the PL AGNs have spectroscopic redshifts compared to 26% of the parent IRAC population. Part of the problem is that the comparatively deep IRAC data probe higher redshifts than the typical redshift of the spectroscopy or the X-ray data. Another problem is that the wavelength range of the DEEP2 observations was chosen to measure galaxies with $z \lesssim 1.4$, and at higher redshifts, typical galaxies show no spectral features observable by DEEP2.⁵ Figure 6 shows that nearly all objects that have spectroscopic redshifts >1.4 are PL AGNs. Redshifts for these sources come from ultraviolet lines that are prominent in AGNs but not in normal galaxies. Furthermore, to have been targeted at all for redshift measurement, galaxies at such high redshifts must be extremely luminous, and such high luminosities in the rest ultraviolet (observed R for DEEP2 selection) are most easily provided by AGNs and moreover *unobscured* AGNs. Indeed, of 26 PL AGNs with DEEP2 spectra,⁶ 15 show strong lines and are classified “AGN.” The automated classifier called the remaining 11 “Galaxy,” but in fact all 11 have emission lines, and at least four have broad lines. Only for three objects are broad lines clearly absent, and the largest redshift for any of these is $z = 1.40$. For the Hectospec redshifts, the target selection mentioned above forces most of the sample to be AGNs, and as expected $>90\%$ of this group was classified that way. The few classified “Galaxy” are all at $z < 1$.⁷ Taking the strong selection effects into account, it is unsurprising that virtually all of the sources observed to have high redshifts are AGNs.

⁵In particular, the $\lambda 3727 \text{ \AA}$ [O II] doublet shifts out of the DEEP2 spectral coverage for $z > 1.4$.

⁶quality 2 for three objects, ≥ 3 for the rest

⁷The Hectospec sample includes one object at $z = 2.18$ classified “Galaxy” by the automated classifier, but inspection (A. Coil 2010, private communication) shows it is really a broad line AGN, and the large redshift is correct.

PL AGNs for which measured redshifts exist tend to have much higher redshifts than the IRAC parent population. The general population of IRAC sources in the DEEP2 redshift survey has a median $z = 0.72$, and the sources observed with Hectospec have median $z = 0.51$. The combined redshift sample has a median $z = 0.68$. Figure 6 shows the redshift distribution. Sixty two of the 489 PL AGNs have high quality spectroscopic redshift measurements, 39 from the Hectospec instrument at the MMT and 23 from the DEEP2 redshift survey using the Keck DEIMOS Spectrometer. The median redshift of these sources is 1.6, and the maximum is 3.5. The PL AGN redshifts are also significantly higher than the median $z = 0.8$ for IRAC sources with X-ray detections. The redshift distribution is relatively flat, suggesting that neither aromatic emission features nor silicate absorption had much effect on sample selection, in contrast to flux-limited $24\ \mu\text{m}$ samples (e.g., Huang et al. 2009). Of the $3.6\text{--}24\ \mu\text{m}$ power-law sources, 20 have redshifts. The median redshift for these sources is again high at $z = 1.6$.

Though the selection effects explain why all the sources with measured high redshifts are AGNs, it is interesting that so many of the spectroscopic high- z AGNs are identifiable as AGNs via their mid-IR properties. In Figure 4, for example, X-ray AGNs exhibit a wide range of mid-IR colors, yet Figure 5 shows that all the AGNs with high measured redshifts are confined within a narrow color range. The reason is likely to be that at high redshift, AGNs are seen and selected for spectroscopy only if they are luminous, and in that case, the power law component is likely to dominate the SED.

6. VISIBLE-TO-MID-INFRARED SEDS

The SEDs of PL AGNs generally do not exhibit the spectral behaviors typical of stellar systems but tend to resemble Type 1 AGNs (e.g., Ramos Almeida et al. 2008, who fit template SEDs to IRAC/X-ray AGNs in the EGS). To compare the SED shapes, Figure 7 shows the SEDs for a sample of randomly selected sources from the general IRAC population in every category of power-law fit. There are 1156 sources that have red-sloping SEDs not fitting a power law; these comprise 10% of the total IRAC population (Table 1). These sources are a diverse group, some showing a stellar bump and others not. Compared to the other three categories of sources, they have a higher rate of reliable redshift measurement. (37% have redshifts as opposed to only 13% of the PL AGNs.) The median redshift of this group is $z = 0.3$, lower than that of any other fit category. Eighty-seven percent of these sources have $z < 0.5$, and only 6% have $z > 1$. These red non-PL objects are far more likely to be detected at $24\ \mu\text{m}$ and $70\ \mu\text{m}$ and have much higher mid-IR flux densities than the other sources. They also have a higher rate of radio flux detection, though their

mean radio flux density is *lower* than that of the other three categories of fit. They have a higher rate of X-ray detection than the blueward sloping sources, though the rate is not as high as seen among the PL AGN sample (see §7.1.1). The majority of these sources are poorly fit to a red power-law because their 4.5 and 5.8 μm flux densities are lower than what a power-law from 3.6–8.0 μm would predict. A plausible explanation for such SEDs is starlight emission, possibly heavily reddened, at 3.6 μm , thermal dust or AGN emission at 8 μm (possibly including PAH emission for low-redshift galaxies), and an SED minimum between these wavelengths where neither component emits strongly. Such an SED is typical of nearby spiral galaxies (e.g., Dale et al. 2005, 2007) or galaxies with starlight contributing most of the light at 3.6 μm but an AGN dominating at 8 μm (e.g., NGC 3079 or 4826 — Lawrence et al. 1985). Thus this group is likely comprised of a mix of relatively low-redshift, starlight-dominated galaxies and AGNs whose IR signatures are diluted or veiled by starlight.

All of the blue sources (85% of the IRAC sample) show a broad emission peak, typically reaching its maximum near 1–2 μm . This is an indication of stellar emission, as shown by the templates in Figure 7. For the 27% of the group with measured redshifts, the mean redshift is 0.73; a range of 0 to 1.5 is consistent with the wavelengths of SED peaks in the group. While some of these sources no doubt host an AGN, its emission is only a minor component at 3.6 μm .

Figure 8 shows SEDs for a selection of PL AGNs. As mentioned above, the PL AGN selection favors optically faint sources, and 18% of the sample do not have *R*-band detections. Of the sources that are detected, 80% have *R*-band flux densities that are more than 50% below the values predicted by the Elvis et al. (1994) template, while 9% have flux densities more than 50% above template values. The X-ray detection rate among the optically brighter sources is high (84%), while the detection among optically fainter sources is only 25%. These optically fainter sources have higher X-ray hardness ratios⁸ ($\text{HR} = -0.1$ compared to $\text{HR} = -0.4$ for the optically brighter sources), suggestive of gas and dust extinction at visible and X-ray wavelengths. Thus the power-law selection appears to be fully capable of finding obscured AGNs.

⁸Hardness ratio $\text{HR} = (H - S)/(H + S)$, where H is the 2–7 keV count rate and S is the 0.5–2 keV count rate. See §7.1.5 for further discussion of hardness ratios.

7. PL AGN MULTIWAVELENGTH PROPERTIES

7.1. X-Ray Properties

7.1.1. X-ray Detection Rate

The power-law selection tends to find sources that have not been identified in X-ray observations, even though PL AGNs have a relatively high X-ray detection rate compared to the general population. Among the sample of 489 PL AGNs, 159 (33%) have X-ray counterparts in at least one band in the 200 ks AEGIS-X catalogs (Laird et al. 2009), which require Poisson false probabilities $< 4 \times 10^{-6}$. (Table 3 summarizes the X-ray detection rates.) The 3.6–24 μm power-law sources have a slightly higher rate of strong X-ray detection with 65 out of 168 (39%) sources having AEGIS-X counterparts. The parent sample of IRAC sources within the *Chandra* field has an X-ray detection rate of only 6%, and the IRAC sources with 24 μm counterparts have an X-ray detection rate of 7%. For comparison, in fields with much deeper X-ray data of ~ 1 Ms, Alonso-Herrero et al. (2006) found that 53% of their power-law galaxies in the CDFS were X-ray detected, while Donley et al. (2007) found an initial detection rate of 55% with Poisson false probabilities $< 1 \times 10^{-7}$ in the CDFN. Thus though deeper X-ray data find more PL AGNs, even the deepest X-ray data available leave a substantial fraction of IR power-law galaxies undetected. More typical X-ray depths of a few hundred ks detect only about half the PL AGNs. Lowering the detection threshold increases the detection fraction but still leaves substantial numbers of PL AGNs undetected. In the EGS, lowering the detection threshold to false probability $< 2 \times 10^{-2}$ (corresponding to 2σ in Gaussian statistics) only raises the X-ray detection rate of PL AGNs to 40%. In the deepest field, the CDFN, 85% of PL AGNs were detected at the 2.5σ significance level (Donley et al. 2007).

The fraction of X-ray-detected PL AGNs does not vary significantly with IRAC spectral slope (see Figure 9). The median IRAC fitted index among the X-ray detected PL AGNs is $\alpha_i = -1.09 \pm 0.05$ compared to the median of $\alpha_i = -1.00 \pm 0.03$ for PL AGNs without X-ray counterparts. For the 3.6–24 μm power-law sources, the median index is $\alpha_m = -0.98 \pm 0.05$ for the X-ray detected sources and $\alpha_m = -1.15 \pm 0.04$ for X-ray non-detected objects.

PL AGNs with X-ray counterparts tend to have higher flux densities in all wavebands than PL AGNs that are not X-ray sources. In particular, the X-ray sources are much more likely to have corresponding visible light detections. (See Figure 10 and §7.3.) The greater rate of visible detections makes X-ray-detected PL AGNs easier to measure spectroscopically than PL AGNs lacking X-ray counterparts, and 1/3 of the X-ray detected PL AGNs (51 sources) have spectroscopic redshifts. The median redshift is $z \approx 1.7$, and 80% of these

sources lie at $z > 1$. In contrast, only 3% (11 sources) of the non-X-ray-detected PL AGNs have measured redshifts. These have a median $z \approx 1.2$, but such a small and likely biased sample cannot yield firm conclusions. The X-ray-detected PL AGNs were specifically targeted by our MMT redshift survey, and therefore at least part of the higher redshift detection rate for those sources is a selection effect, but the difference in fluxes is real. The higher fluxes for X-ray sources must be due to some combination of smaller distances, lower obscurations, and/or higher intrinsic luminosities. For example, the process that fuels X-rays might also produce visible light. The overall similarity of the average SEDs (Fig. 10) tends to suggest that there is little differential obscuration *affecting the infrared emission*, though the fact that observed SEDs fall below the AGN template in the visible and ultraviolet suggests that obscuration is present in both classes. However, infrared slopes do not seem to predict X-ray obscuration (§7.1.5), and stacking of undetected sources (see §7.1.2) suggests that differential obscuration is at least part of the story. Nevertheless, greater distance could also be important despite the few available redshifts being low. If distance were the only factor, the X-ray-undetected sources would have to have redshifts of order 2.5 (taking the K-correction into account) to match the SED of the X-ray-detected sources.

7.1.2. X-Ray Stacking

Stacking is a powerful way to examine the emission properties of sources too faint to be identified individually (Georgakakis et al. 2008). There are 330 PL AGNs that do not have strong X-ray counterparts in the AEGIS-X catalog. Removing 17 objects potentially contaminated by a bright, nearby X-ray source leaves 313 stackable sources. Stacking X-ray counts (with the same methods used Georgakakis et al. 2008 including the same $2''$ radius) yields significant detections in both the soft and hard bands at a level $>10\sigma$. The stacked soft band flux is $(2.37 \pm 0.31) \times 10^{-17}$ erg cm $^{-2}$ s $^{-1}$, and the stacked hard band flux is $(1.35 \pm 0.20) \times 10^{-16}$ erg cm $^{-2}$ s $^{-1}$. These values are about 1/3 to 1/2 of the thresholds for individual detection. In order to ensure that the stacked signal is not due to an unequal contribution from a few X-ray sources that just missed being included in the AEGIS-X catalog, we stacked again after removing the weakly-detected X-ray sources. There is still X-ray emission at 5σ above background: soft band flux $(1.09 \pm 0.30) \times 10^{-17}$ erg cm $^{-2}$ s $^{-1}$ and hard band flux $(8.10 \pm 2.09) \times 10^{-17}$ erg cm $^{-2}$ s $^{-1}$. Thus the stacked emission appears to be representative of the undetected population rather than dominated by a few moderately bright X-ray sources, consistent with results in fields with much deeper X-ray data (Alonso-Herrero et al. 2006; Donley et al. 2007).

The spectrum of the stacked signal is relatively hard with $HR = 0.05 \pm 0.10$. After

weakly-detected sources are removed, the spectral slope of the remaining stack is likewise hard with $\text{HR} = 0.18 \pm 0.18$. Assuming the average stacked source has $z = 1.6$ (equal to the median redshift of the PL AGN sample), the hardness ratio can be used to estimate obscuration by calculating column densities using the PIMMS tool available from CIAO (v3.9b, Mukai 1993). The result is $N_{\text{H}} \sim 10^{23} \text{ cm}^{-2}$ (assuming a power-law model with intrinsic $\Gamma = 1.9$), implying a high but not Compton-thick level of obscuration. The hardness ratio is also consistent with a nearly flat X-ray spectrum, $\Gamma \sim 1$, which can be interpreted as evidence for a large fraction of Compton-thick AGNs among the X-ray-undetected PL sources. In this picture, the direct emission from the AGN is fully absorbed, and the observed X-rays come from reflection off the torus or the accretion disk (Gilli et al. 2007). The reflected component has a very flat spectrum, $\Gamma \lesssim 1$ (George & Fabian 1991; Matt et al. 2000), and does not provide any information about the actual N_{H} , just that the source is likely to be Compton-thick. The HR alone cannot discriminate between these possibilities or in general between Compton-thick or Compton-thin obscuration. Moreover, sources below but close to the Compton-thick limit may still be reflection-dominated in the *Chandra* and XMM bands (depending on redshift), further complicating the interpretation. Whatever the explanation for the hard spectrum may be, the hardness doesn’t depend on whether or not the weakly-detected sources are included in the stacking.

One possible way to discriminate between Compton-thick and Compton-thin obscuration is to compare hard X-ray and infrared fluxes. These two quantities are well correlated for AGNs with low to moderate obscuration as first recognized by Carleton et al. (1987) and studied in more detail by Lutz et al. (2004). Figure 11 shows the comparison for the PL AGN sample. The X-ray-detected objects fall within or near the Lutz et al. relation, even without correcting the X-ray fluxes for any absorption. In contrast, the stacking signal for the X-ray undetected PL AGNs is more than 100 times fainter than the relation, consistent with Compton-thick absorption. Stacking gives no information about individual objects, but if some have relatively large X-ray fluxes and are therefore not Compton-thick, the rest must have even smaller fluxes and be further into the Compton-thick zone. Thus it seems likely that many, perhaps a majority, of the X-ray-undetected PL AGNs suffer Compton-thick obscuration. Fiore et al. (2009), using a different selection of infrared sources, also found large numbers of X-ray-undetected, Compton-thick AGNs.

Another issue is the depth of the X-ray coverage. Georgantopoulos et al. (2008) conducted an X-ray stacking analysis of IRAC sources in the CDF-N, which has even deeper IRAC data than the EGS. They found that color-selected sources in the Stern et al. AGN wedge produce a soft spectrum consistent with $\Gamma \sim 2.1$, whereas power-law sources produce a harder signal ($\Gamma \sim 1.6$) as expected of AGNs. Our stacking analysis (§7.1.2) shows that in the EGS, sources in the Lacy et al.-defined wedge, sources in the Stern et al. wedge, and PL

AGNs all have similar stacked fluxes and are all relatively hard with $HR \approx -0.2, -0.1$, and 0 respectively.⁹ The difference in results is likely to be due to X-ray depth of fields: more of the faint X-ray sources are detected by the very deep exposures of the CDF-N and excluded from the stacking analysis, whereas in the shallower EGS, sources at similar X-ray fluxes remain undetected and therefore are included in the stacked flux. These results suggest that many of the X-ray-undetected sources in the Lacy and Stern selection in the EGS *would* be detected with 2 Ms X-ray data. However, the soft spectra of the fainter X-ray sources in the CDF-N suggests that the color-wedge-selected samples at EGS-like depths have a high rate of contamination from ULIRGs and other star-forming galaxies, as expected from the behavior of template colors with redshift (§4.1).

7.1.3. Comparison of X-ray and PL AGN Populations

PL AGNs represent 22% of the X-ray sources in the EGS. This is much higher than the 4% PL AGNs in the general IRAC parent sample, but sources with red IRAC power law SEDs are still a minority of X-ray objects. Relaxing the power-law definition to $P(\chi^2) \geq 0.01$ and $\alpha_i \leq 0$ increases the fraction to 40%, as found by Barmby et al. (2006) with that definition. A comparable selection rate was also found by Cardamone et al. (2008) among their sample of X-ray sources with $L_X \geq 10^{42}$ erg s⁻¹ in the ECDFS using the definition $\alpha_i \leq 0$ and $P(\chi^2) \geq 0.05$. Because most X-ray sources in the EGS are expected to be AGNs, requiring a red IRAC power-law SED will not identify even a majority of active nuclei.

The respective X-ray and PL AGN detection fractions can be estimated under the assumption that the two methods are observing a single AGN population and that detection by each method is *independent* of the other. Each method then detects a fixed fraction of the population, and the product of the detection fractions times the number in the population is the 159 X-ray-detected PL AGNs.¹⁰ The resulting detection fractions are 0.33 for X-ray, 0.22 for PL AGNs, and the population size is 2200 objects. The assumption of a single population is probably wrong because the EGS infrared observations reach higher redshifts than the X-ray observations. The effect of this error is that the X-ray population is likely to be smaller and detection fraction larger than estimated above. Perfect independence of detection is also doubtful, despite the most likely reasons for non-detection being entirely

⁹Stacking for each wedge included all the IRAC sources not detected as individual X-ray sources. About 5% of the stacked sources in the Lacy et al. and about $\sim 20\%$ in the Stern et al. wedge are PL AGNs. See §4.1 for other statistics on the wedge populations.

¹⁰Harwit (1981) discussed the statistical method and assumptions.

different for the two methods (extinction for the X-rays, additional contaminating radiation sources for the infrared), because higher luminosity sources are more likely both to overcome extinction and to outshine contaminating sources. The effect of this error is that both detection fractions are overestimated and the overall population size is underestimated. Thus the specific numbers above are at best rough estimates, but the method is still useful for comparing AGN populations found by different surveys.

Our study finds fewer X-ray sources with blue power law SEDs than previous studies have, but this is at least partly because our power law selection is more stringent. According to our criteria, only 19% of X-ray sources fit a blue power law in the IRAC bands. Relaxing the criteria to those used by Barmby et al. (2006) increases the fraction to 23%, but this is still much smaller than the 38% found by Barmby et al. The discrepancy is mostly because the observational error bars at 3.6 and 4.5 μm are smaller in the final catalog (Barmby et al. 2008) used here than in the earlier catalog used by Barmby et al. (2006).¹¹ Cardamone et al. (2008) found 59% of X-ray counterparts fit a blue power law in the IRAC bands, but they included sources with detection significance as low as 3σ instead of the 5σ we required. With large photometric error bars, a power law will adequately fit many more sources. Indeed Cardamone et al. found 97% of X-ray sources and 94% of all IRAC sources fit a power law versus our values of 41% and 34% respectively. Regardless of the exact numbers, the presence of X-ray sources among this group means that a blue SED, even one closely fitting a power law in the IRAC bands, does not rule out the presence of strong nuclear activity.

Requiring a power law fit from 3.6–24 μm yields an even smaller percentage of X-ray objects: only 10% of sources with 24 μm and X-ray detections fit a red power-law from 3.6 to 24 μm (using our original cut of $P(\chi^2) \geq 0.1$ and $\alpha_m \leq -0.5$). However, while the X-ray sources with IRAC power laws are roughly evenly divided between red and blue power-law sources, X-ray sources that fit a 3.6–24 μm power law are virtually all red. (See Figure 3.) Of the 70 3.6–24 μm power-law sources with X-ray counterparts, only 5 exhibited the blue power laws indicative of stellar emission. This is hardly surprising given the detection limits of the surveys; very few sources will be detectable at 24 μm unless the 24- μm flux density is considerably larger than the 8- μm flux density.

7.1.4. X-ray Luminosity

Rest-frame luminosity is a useful diagnostic of the power source for an X-ray-emitting galaxy (Barger et al. 2002). Rest-frame hard band (2–10 keV) X-ray luminosities were

¹¹Systematic magnitude offsets between the two catalogs are only a few percent and thus insignificant.

calculated for the 47 sources with hard band detections and spectroscopic redshifts using $L_X = 4\pi d_L^2 f_X (1+z)^{\Gamma-2} \text{ erg s}^{-1}$, where d_L is the luminosity distance calculated from Equation 1 of Pen (1999), and f_X is the hard band flux in units of $\text{erg cm}^{-2} \text{ s}^{-1}$. Most of these spectroscopically confirmed sources appear to be obscured but not Compton thick (see §7.1.5 and Fig. 11), so we have assumed an intrinsic photon index of $\Gamma = 1.9$ (Nandra & Pounds 1994) for which the effects of absorption and K-correction should be minimal (Barger et al. 2002). All of these sources have X-ray luminosities $L_X > 10^{43} \text{ erg s}^{-1}$ with a maximum luminosity of $L_X \sim 10^{45} \text{ erg s}^{-1}$. Such high luminosities are typical of AGNs. This is further confirmation that our sample is not likely to be dominated by star-formation, as L_X values of local starburst systems typically lie below $10^{42} \text{ erg s}^{-1}$ (Barger et al. 2002). As expected (Alonso-Herrero et al. 2006; Donley et al. 2008), virtually all of the highest X-ray luminosity sources are PL AGNs (see Figure 12), and 35 out of the 50 sources with $L_X > 10^{44} \text{ erg s}^{-1}$ are PL AGNs. Of the 15 exceptions, 12 have red-sloping IRAC SEDs but were excluded by our goodness-of-fit criteria. One source was well fit to a blue power law with $\alpha_i \sim 0.3$, and two sources were poorly fit to a blue power law with $-0.3 < \alpha_i < -0.5$. Thus, although only a minority (22%) of X-ray sources are PL AGNs, the majority (70%) of the most X-ray-luminous objects are in this class. The remaining 30% of highly luminous X-ray sources are likely AGNs with contamination from stars and dust in the host galaxy preventing their identification via the power-law selection.

A hard X-ray luminosity of $0.5 - 1 \times 10^{44} \text{ erg s}^{-1}$ marks a division between PL AGNs and blue power-law sources (Figure 12). This luminosity is near the break (L^*) in the X-ray luminosity function at our median sample redshift of $z \sim 1.6$ (Ueda et al. 2003; Silverman et al. 2008). PL AGNs having X-ray luminosities below the break value are not excluded by low X-ray fluxes (as shown by the stacking analysis) but rather by the absence of redshifts. The high X-ray luminosity for galaxies detected as PL AGNs suggests that the PL AGNs without X-ray counterparts are either very distant compared to the sources with X-ray detections or else heavily obscured. Though the physical interpretation behind the break in the luminosity function is still unclear, the power-law selection may be finding an AGN population that is distinct from the sub- L^* X-ray galaxies. The sub- L^* X-ray population may include AGNs with little dust near the nucleus or different accretion modes (and hence lower intrinsic near-IR emission) or AGNs veiled by emission from the host galaxy (and hence not identified as an AGN by the near-IR SED).

Veiling by the host galaxy is probably at least part of the reason PL AGNs with low luminosities are uncommon (Donley et al. 2007). Figure 13 shows the relation between hard X-ray flux and IR flux at different wavelengths. Among sources that exhibit both X-ray emission and PL AGN SED shape, there is a strong linear correlation between X-ray and IR flux. This implies that PL AGNs are dominated by nuclear emission (as demonstrated by

Carleton et al. 1987), with both X-ray and IR light closely related to the central engine. In contrast, the sources with IRAC and X-ray detections and spectroscopic redshifts but that are not PL AGNs show much weaker correlation between IR and X-rays. Indeed, the $3.6\ \mu\text{m}$ flux for this sample is essentially constant, suggesting that in the non-PL AGN sources, $3.6\ \mu\text{m}$ emission arises from a source unrelated to the central engine. Stellar emission from the host galaxy is the obvious candidate. In this picture, low-luminosity AGNs are only identified as PL AGNs if they happen to reside in a low-luminosity host galaxy.

7.1.5. *X-ray Hardness and Obscuration*

If the PL AGN sample preferentially selects sources that are obscured at X-ray energies, one might expect the X-ray hardness ratio to be greater for the PL AGN sample than the parent population. However, PL AGNs do not appear to exhibit significantly harder ratios than the general sample (Figure 14). One-third of the PL AGNs with strong detections in both the hard and soft bands are considered hard with $\text{HR} > -0.2$ (e.g., Szokoly et al. 2004). Of sources detected in at least one band, the median $\text{HR} = -0.30$, and 40% have $\text{HR} > -0.2$. Weakly detected sources are harder with a median $\text{HR} = 0.15$ and 72% having $\text{HR} > -0.2$. The harder X-ray spectra suggest that the X-ray-weak PL AGNs are more obscured than PL AGNs with strong X-ray detections. However, the correlation coefficient between the IRAC power-law slope and the X-ray HR is essentially zero, suggesting either little difference in obscuration or that obscuration has little effect on the IRAC slope. PL selection seems to detect X-ray obscured and unobscured objects more or less equally well, without a strong preference for one or the other. If this is so, the power-law selection technique can be a way of identifying objects that are hidden behind gas and dust and therefore missed by other surveys.

Figure 14 shows little if any correlation between X-ray hardness and infrared slope for PL AGNs. Either the infrared slope is controlled by properties other than extinction or the material responsible for infrared extinction is not the same as the material responsible for X-ray obscuration.

There are 46 PL AGNs with spectroscopic redshifts that have been strongly detected in both the hard and soft bands for which the column density can be estimated using PIMMS. Of these, 90% are obscured with column densities $N_{\text{H}} > 10^{22}\ \text{cm}^{-2}$. Two sources (EGSPL 80/153) have hardness ratios consistent with being Compton thick ($N_{\text{H}} > 10^{24}\ \text{cm}^{-2}$), but the ratios of X-ray to $5.8\ \mu\text{m}$ flux (among the red squares in Fig. 11) indicate less obscuration than this. Probably these sources have high but not Compton-thick obscuration, perhaps with a harder-than-average intrinsic spectrum. Another atypical source could not be

fit using $\Gamma = 1.9$ and appears to require a steeper intrinsic slope to get the observed counts. All column density values here are uncertain because errors in hardness ratios can be large, and reliable estimates of obscuration levels will require proper spectral fitting analysis (Laird et al. 2006). Indeed the simple obscuring slab geometry assumed in the calculations may not apply at all (La Massa et al. 2009). Nevertheless, the hardness ratios and column density calculations suggest a high amount of obscuration among the X-ray sources, but none of the *detected* sources is likely to be Compton thick (Fig. 11).

7.2. Infrared Properties

7.2.1. 24–70 μm Flux Densities

Among the PL AGN sample, 399 (82%) have 24 μm counterparts within $1''.5$. Some of the PL AGNs may have escaped 24 μm detection because of the 9.7 μm silicate absorption feature, which is commonly seen in absorbed AGNs (Rieke & Low 1975; Roche et al. 1991). The absorption band will be redshifted to 24 μm at $z \sim 1.5$, near our median redshift value.

Many IR luminous galaxies are thought to host AGNs, and Weedman et al. (2006) and Brand et al. (2006) demonstrated that the AGN fraction in 24 μm -selected samples tends to increase as 24 μm flux density increases from 0.1 to 1 mJy. Yet 57% of the PL AGNs with 24 μm counterparts have $S_{24} < 100 \mu\text{Jy}$, and only 4% have flux densities exceeding 1 mJy (see Fig. 15 for the distribution of flux densities). The median 24 μm flux density of the PL AGN sample is in fact smaller than the median of the entire IRAC/MIPS population because the power-law selection excludes strong star forming systems, which are bright in the mid-IR. In agreement with Donley et al. (2007), the 24 μm detection fraction is high (100%) for objects with X-ray luminosity $L_X \approx 10^{41} \text{ erg s}^{-1}$. The X-ray emission in these relatively weak X-ray sources is likely to come from stellar processes rather than an AGN. Near $L_X \approx 10^{42} \text{ erg s}^{-1}$, the 24- μm detection fraction drops to $\sim 80\%$, but it rises again to 100% with increasing X-ray luminosity. Thus 24 μm is not a particularly efficient wavelength to search for AGN emission, but AGNs generally will emit at that wavelength in accordance with the power-law character of their SEDs (Elvis et al. 1994). The relative depths of the X-ray and 24- μm surveys in the EGS mean nearly all X-ray AGNs are detected at 24 μm .

Extending the IRAC power law to 24 μm is not a good predictor of actual 24 μm flux density for individual objects, as noted by Barmby et al. (2006). Only 11% of PL AGNs with 24 μm detections have actual 24 μm flux density within 10% of the value predicted by extrapolating the IRAC power law. In our sample, the extrapolated 24 μm flux density is greater than the actual flux density 40% of the time and less than the actual flux density 60%

of the time. While the power law character of the SED is a good approximation statistically, actual SEDs show breaks in the (observed) 3.6–24 μm range as would be found for local QSOs (Netzer et al. 2007) if they were observed at redshifts characteristic of the PL AGN sample.

Only eight PL AGNs have a detection at 70 μm . These sources have atypically high S_{24}/S_{70} ratios compared to the parent sample, but this SED is consistent with the expected AGN energy distributions (Elvis et al. 1994).

7.2.2. Variability

Because AGNs are so compact, they can vary on short timescales. Kozłowski et al. (2010) found typical AGN variability at IRAC wavelengths to be about 0.05 mag in six months, though of course individual objects can vary more or less than this amount. The IRAC EGS data were taken in two epochs: 2003 December and 2004 June–July (Barmby et al. 2008), and we have analyzed the two epochs separately to check for flux variability. Variability was defined such that $|\Delta S|/\delta S > 4$, where ΔS is the difference in flux density between the two epochs and δS is the quadrature sum of the individual measurement uncertainties. The probability of random observational errors causing a constant source to vary by 4σ in one IRAC bandpass is 6×10^{-5} . In the full sample of 11787 IRAC sources, less than one source would be expected to show spurious variation at this level in one bandpass and a negligible fraction in all four bandpasses.

Among our 489 PL AGNs, 397 were separately detected in both the epoch 1 and epoch 2 catalogs. Two sources ($\sim 1\%$) were reliably observed to vary in the mid-IR by $>4\sigma$ in all bandpasses: EGSPL 122 increased in flux density at all four wavelengths from 2003 to 2004, while EGSPL 153 decreased at all wavelengths. Both sources have flux densities $\gtrsim 100 \mu\text{Jy}$ in the four IRAC bandpasses (AB magnitudes 17–18), 15–60 times higher than the median flux densities for the PL AGN sample. The actual variation over the 6 months amounted to a difference of about 10%, easily detectable with the large S/N . Both sources have X-ray counterparts, as expected for bright AGN.

A third source (EGSPL 35) showed more complex brightness variations. This source has IRAC flux densities 400–700 μJy (AB magnitude 16–17). It also varied by $>4\sigma$ across all four IRAC bandpasses, but it increased its flux density at 3.6 μm and 5.8 μm while decreasing at 4.5 μm and 8.0 μm . (There are no obvious image artifacts near this or any of the variable sources in the PL AGN sample.) IRAC observes wavelengths 3.6 μm and 5.8 μm simultaneously and wavelengths 4.5 μm and 8.0 μm simultaneously. In 2003 December,

approximately 21 hours passed between the 3.6/5.8 μm observations and the 4.5/8.0 μm observations of EGSPL 35. Thus, it is possible that these observations may have caught a brief infrared flare.

Lowering our variability threshold to 3σ results in only one additional PL AGN varying across all four channels. However, $\sim 51\%$ of our PL AGNs varied by 3σ in at least one IRAC channel, and $\sim 32\%$ varied by 4σ in at least one channel. The high incidence of apparent variability is further confirmation of the AGN character of the PL AGN sample.

Though the number of variable PL AGNs is too few to make statistical comparisons to the parent sample, there were 15 sources (including the two PL AGNs) in the IRAC population with consistently increasing or decreasing flux densities across all four IRAC channels between the two epochs. Forty percent of these are identified as AGNs via their X-ray emission and are thus likely to be real variables. The rate of detecting a non-X-ray source that varies in the IR is therefore $\lesssim 0.1\%$ in our data, suggesting that photometric failures causing spurious variability are minimal. Thus variability appears to be real and characteristic of AGNs, as found by Kozłowski et al. (2010). As also shown by those authors, even four epochs are not sufficient to find a majority of the variable population, and two epochs as here will be even less complete.

7.3. Visible Light Properties

PL AGNs have a lower rate of visible light detection compared to the parent sample of IRAC sources, and the detections tend to be fainter (median $R_{AB} = 24.5$ versus 23.0).¹² The relative faintness in visible light is expected if the IRAC power-law extends even roughly into the near-IR and visible bands, as many do (see §6). Eighteen percent of our sample is optically faint and not detected by Subaru down to a limit of $R \sim 26.5$ at 5σ or CFHT down to a limit of $R \approx 24.2$ at 8σ as compared to 9% of the parent IRAC sample being undetected at R . Figure 16 shows the distribution of R -band magnitudes for the PL AGN sample.

X-ray to visible (“optical”) ratios (X/O) are commonly used to separate AGNs from starburst galaxies (Maccacaro et al. 1988; Alexander et al. 2001; Hornschemeier et al. 2001; Barger et al. 2003) and are defined as $X/O = (R/2.5) + 5.5 + \log(F_{\text{HB}})$ where R is the R -band magnitude (Vega) and F_{HB} is the X-ray hard band flux. Because AGNs are powerful enough to fuel energetic X-rays, they are expected to have high X/O , 0.1–10 or greater.

¹²As throughout this paper, the IRAC parent sample includes only sources detected in all four bands with $S/N > 5$.

$X/O \sim 0.01\text{--}0.1$ generally indicates low luminosity AGNs or galaxies dominated by star formation, and even lower X/O is characteristic of normal galaxies, which have very weak hard X-ray emission. At the depth of our data, nearly all detected X-ray sources are expected to be AGNs, and indeed 95% of the X-ray plus IRAC sample have $X/O > 0.1$. There are 116 PL AGNs that have both optical R band detections and strong X-ray hard band detections; this is 95% of all hard band detected PL AGNs. All of these have X/O consistent with values expected for AGNs (see Figure 17). The X-ray stacked source also lies in the AGN region, though outside the limits of the plot. In general, PL AGNs with X-ray detections are optically brighter than sources without X-ray detections (see Figure 18). This is consistent with the X-ray-detected population being at lower redshift, less obscured, or both.

Nearly a quarter of the PL AGNs with both R and X-ray detections have extreme X-ray to optical ratios of $X/O > 10$ (Fig 17). In many of these, the ratio is large because the objects are quite faint in R band rather than because they have stronger X-ray fluxes than average. Objects with large X/O ratios are candidates for being at high redshift and Compton thick (Civano et al. 2005), though Compton-thick seems unlikely for any of the X-ray-detected objects because of the observed X-ray to infrared ratios (Fig. 11). Sources with $X/O > 10$ have a median hardness ratio of $HR \sim 0$, compared to the median of $HR = -0.3$ among all of the X-ray-detected PL AGNs. Less than half of these sources have available *HST*/ACS observations, and of these most are too faint to determine morphology by eye. However, three sources appear extended while one appears point-like. Beyond their identification as AGNs, the nature of the extreme X/O sources remains in doubt.

Pierce et al. (2007) observed the host galaxy morphologies of IRAC power-law objects with $\alpha_i < 0$ within the redshift range $0.1 < z < 1.2$ and found that X-ray selected AGNs lie mostly in E/S0/Sa hosts and not in Sc/Sd/Irr galaxies. Conversely, PL AGNs without X-ray detection inhabit host galaxies of all types, though the selection may work against AGNs hosted by E/S0/Sa galaxies. Because X-ray undetected PL AGNs are optically very faint, it is difficult to obtain morphologies for these sources, and those lacking redshifts were not included in the Pierce et al. (2007) sample at all. However, Figure 18 suggests that X-ray-detected PL AGNs and X-ray undetected PL AGNs may inhabit morphologically different galaxies. Undetected PL AGNs may be surrounded by dust and gas, which obscure both the visible light and the X-ray emission. Emission from the dust could contribute to emission at $24\text{ }\mu\text{m}$ and longer wavelengths. The morphological difference suggests that obscuration is at least part of the reason for many PL AGNs not being detected in X-rays, but higher redshifts could well be important too.

7.4. Radio Properties

The VLA observations cover roughly two-thirds of the IRAC + *Chandra* field. Of the 357 PL AGNs within the radio field and outside of high-noise regions, 31 ($\sim 9\%$) have 1.4 GHz counterparts with $S/N > 5$. Over half of these have flux densities $S_{1.4 \text{ GHz}} < 100 \mu\text{Jy}$, and over 75% have $S_{1.4 \text{ GHz}} < 200 \mu\text{Jy}$ (see Figure 19). Four sources (13%) have $S_{1.4 \text{ GHz}} > 1 \text{ mJy}$. This is higher than the $\sim 5\%$ of all radio sources that have $S_{1.4 \text{ GHz}} > 1 \text{ mJy}$, though barely statistically significant. However, 1/4 of galaxies with $S_{1.4 \text{ GHz}} > 1 \text{ mJy}$ are PL AGNs. One source (EGSPL 260) is very radio-bright with $S_{1.4 \text{ GHz}} \approx 10 \text{ mJy}$. This source is considerably brighter in all observed wavebands than the respective median flux densities: it has $S_{24} \approx 1.25 \text{ mJy}$ and an X-ray detection that is ~ 10 times higher than the median X-ray flux observed for *Chandra* sources (but near the median X-ray flux for the PL AGN sample). ACS morphology shows that the source is point-like, but no redshift has yet been measured for this object.

The ratio of radio to 24 μm flux densities can be used as a sign of AGN emission. All but one of the PL AGNs with radio counterparts also have detections in the 24 μm band, allowing us to study the ratio between the radio and mid-IR flux densities using $q \equiv \log(S_{24}/S_{1.4 \text{ GHz}})$. Star-forming systems show a strong correlation between radio and far infrared flux densities (Condon 1992), and this correlation extends to 24 μm (Appleton et al. 2004). Rieke et al. (2009) discussed measurements of q for local star-forming galaxies and found $q \gtrsim 1.22$, but the value of q at a fixed observed wavelength depends on redshift. Lacking redshifts for most of the PL AGNs, we stick to observed flux densities rather than attempt uncertain K corrections, and the most suitable comparison is $q = 0.84 \pm 0.28$ (Appleton et al. 2004). Sources with $q < 0$ have strong radio emission relative to their 24 μm flux densities and are considered radio-loud AGNs (Donley et al. 2005; Park et al. 2008). Eleven out of the 30 PL AGNs (37%) with both radio and 24 μm detections have $q < 0$. This is somewhat higher than the 20% of sources in the EGS radio/IRAC sample that have $q < 0$, and also higher than the fraction found by Donley et al. (2007), who found that only 2 out of their 18 power-law sources had $q < 0$. However, the small-number statistics and different radio depths of the EGS and GOODS fields make any detailed comparison problematic. An additional ten PL AGNs have $0 < q < 0.56$, outside the range expected for star formation but not quite in the radio-loud category. The remaining 9 radio/24 μm /PL AGNs have q values within the expected range for star-forming galaxies and non-radio-excess AGN with the largest value being $q = 1.26$.

Only four of the radio-detected PL AGNs have redshifts, and luminosities have been calculated for these sources assuming a radio spectral index of $\alpha = 0.8$ (Yun et al. 2001). Two sources had $L_{1.4 \text{ GHz}} > 10^{24} \text{ W Hz}^{-1}$ at redshifts of 1.4 and 1.7, while two had $L_{1.4 \text{ GHz}} \sim 2\text{--}$

$4 \times 10^{23} \text{ W Hz}^{-1}$ at redshifts of 0.5 and 1. These luminosities are consistent with values observed for AGN radio sources in the local universe, which typically have $L_{\text{radio}} > 10^{23} \text{ W Hz}^{-1}$ (Yun et al. 2001). IRAC sources that are not PL AGNs but do have radio counterparts have a median redshift of $z = 0.6$ and median luminosity of $L_{1.4 \text{ GHz}} \sim 10^{23} \text{ W Hz}^{-1}$. These could be either AGNs or luminous starbursts.

A stacking analysis of the PL AGNs without radio detections yields significant detection ($S/N > 20$) with a median 1.4 GHz flux density of $13.5 \pm 0.7 \mu\text{Jy}$ per beam after accounting for bandwidth smearing, stacking losses, and stacking bias. Assuming the stacked source is at the median redshift $z = 1.6$, it would have a luminosity of $L_{1.4 \text{ GHz}} = 1.9 \times 10^{23} \text{ W Hz}^{-1}$, well within the AGN range (e.g., Yun et al. 2001). If this stacked source were powered by star formation, its luminosity would translate to a star formation rate of $>200 \text{ M}_{\odot} \text{ yr}^{-1}$ for a Salpeter IMF. Thus explaining the radio emission for much of the sample by star formation requires a high star formation rate; an AGN attribution seems more likely. A q value for the stacked source can be estimated using the median $24 \mu\text{m}$ flux density for the PL AGN sample, $86 \mu\text{Jy}$, giving $q = 0.8$ and implying that few if any of the radio-undetected sources can be radio-loud AGNs. Thus the radio-loud fraction of the PL AGN population is $11 \text{ } q < 0$ detected sources out of 357 PL AGNs in the radio area, $\lesssim 5\%$. This fraction is typical of other AGN surveys (e.g., Green et al. 2009)¹³ and again consistent with the AGN character of the PL AGN sample.

Ten of the 30 PL AGN radio sources have X-ray counterparts. This fraction is consistent with expectations from a study of q -selected sources in the general IRAC/X-ray/radio source population (Park et al. 2008). EGSPL 260, the bright radio source mentioned above, has an X-ray counterpart, but among the rest of the sources in the small sample, the presence of X-ray counterparts does not appear to be correlated with the radio flux densities, as shown in Figure 20. The PL AGN sample in general lies closer to the AGN correlation than do other X-ray and radio sources, although there is one PL AGN source near the starburst correlation line. (This is again EGSPL 260.) The majority of the sources lie between $100 < S_{1.4 \text{ GHz}} < 300 \mu\text{Jy}$, and these modest radio sources tend to show X-ray emission above the starburst correlation. The clustering of sources at low radio flux densities and low X-ray fluxes may be an indication of X-ray absorption and the limits of our survey rather than an inherent attribute of these sources. As Simpson et al. (2006) noted, the starburst and AGN correlations shown in Figure 20 may be overestimates; they are derived by using a relatively deep radio survey and a relatively shallow X-ray survey. Hence, the

¹³Determining the fraction of the AGN population that is radio loud is complex and controversial, and the result likely depends on luminosity and redshift. Jiang et al. (2007) and Rafter, Crenshaw, & Wiita (2009) provide recent overviews.

true correlation may actually lie lower than plotted and include more of the population than currently indicated. This would be consistent with the X-ray emission from PL AGNs being primarily produced by the nucleus, rather than star formation, as also argued in §7.1.4.

8. SUMMARY

The IRAC power-law selection technique is designed to identify sources that are dominated by AGN emission in the infrared bands regardless of obscuration. Only 4% of the IRAC sources and 2% of the IRAC/MIPS sources in the EGS are identified as power-law AGNs using our criteria. PL AGNs have SEDs that generally follow AGN templates with either a rough power-law shape from IRAC to visible wavelengths or a downturn in flux density at the visible wavelengths. This may be due to gas and dust obscuring the visible light from PL AGNs. PL AGNs by definition exhibit no SED ‘bumps’. This is unlike much of the rest of the IRAC parent population, which often show clear stellar emission features in their SEDs.

PL AGNs typically have low visible flux densities but are highly luminous overall. Most of the luminous X-ray sources ($L_x \geq 10^{43}$ erg s $^{-1}$) in the EGS are PL AGNs. The high luminosity of PL AGNs allows their detection at high redshifts, and indeed the EGS PL AGNs lie at a median redshift of $z \sim 1.6$, much higher than the median redshift of $z \sim 0.7$ of the parent IRAC population.

One-third of the PL AGN sample have X-ray counterparts, a detection rate greater than the 6% found for the parent population. The detection fraction rises slightly if low-significance X-ray detections are included. However, among all X-ray-detected IRAC sources, only about one-fifth exhibit red power-law SEDs, while a similar fraction exhibit blue power-law SEDs (with spectral index $\alpha_i > -0.5$); the rest are not well fit by a power law. As most of the X-ray sources in our field are expected to be AGNs, the lack of a red power law in the IRAC bands is not an indication of inactivity in a galaxy. Rather, the power-law method finds energetically dominant AGNs and leaves out sources with host galaxy stellar contributions rivaling or exceeding the AGN infrared light. There is a clear division between red power-law sources and blue power-law sources near the break luminosity in the X-ray luminosity function at $L_X \sim 10^{44}$ erg s $^{-1}$, suggesting a physical transition from sources dominated by host galaxy light to those dominated by nuclear emission. While fewer than half the PL AGNs are individually detectable in X-rays with 200 ks *Chandra* exposures, an X-ray stacking analysis found a significant X-ray signal for the rest. Among the X-ray-detected sources with secure redshifts, most of the sources are obscured with $N_H > 10^{22}$ cm $^{-2}$, but none is likely to be Compton-thick with $N_H > 10^{24}$ cm $^{-2}$. Assuming the stacked source has

a redshift equal to the median, the observed hardness ratio corresponds to a column density of 10^{23} cm^{-2} , but the ratio of mid-infrared to X-ray fluxes for the stacked source implies that a substantial fraction of the undetected sources are Compton thick.

Eighty-two percent of the PL AGN sample have $24 \mu\text{m}$ counterparts. Though the AGN fraction in other samples increases with higher $24 \mu\text{m}$ flux densities, the majority of our PL AGNs are not especially mid-IR luminous with 57% of them having $S_{24} < 100 \mu\text{Jy}$. The IRAC power law cannot be extended to predict observed $24 \mu\text{m}$ flux density — only 11% of PL AGNs have IRAC power laws that extrapolate to $24 \mu\text{m}$ flux densities within 10% of the actual values.

In two epochs separated by six months, there are only mild indications of infrared flux variability in the PL AGN sample. While about one-third of the PL AGNs varied by at least 4σ in at least one IRAC band, only a few objects exhibited variability exceeding 4σ across all four IRAC bandpasses. These results are consistent with other studies of AGN variability, but the number of epochs is too small to make definitive conclusions about infrared variability in particular.

Though the power-law selection tends to identify optically-faint galaxies, 82% of the PL AGNs have R -band detections. All sources with both R -band and hard X-ray detections have X-ray/optical ratios of 0.1 or greater, consistent with values expected for AGNs. Nine percent of the PL AGNs have 1.4 GHz counterparts. Half of these have $S_{1.4 \text{ GHz}} < 100 \mu\text{Jy}$, suggesting that PL AGNs are not preferentially radio-bright. Nearly forty percent of the PL AGNs with radio counterparts have $q \equiv \log(S_{24}/S_{1.4 \text{ GHz}}) < 0$. These sources have radio-to-mid-infrared flux ratios higher than typical for star-forming galaxies and can be characterized as ‘radio-loud’; however they make up only a small fraction of the overall PL AGN sample.

Ultimately, to uncover the mysteries of galaxy formation and evolution, a complete and reliable census of AGNs must be obtained for study. To develop such a census, we must discover what types of sources are identified by all of the various AGN selection techniques. The power-law selection method returns highly luminous, often obscured, nuclear-dominated galaxies at intermediate to high redshifts. The method is not intended to select all AGNs or even all infrared AGNs; a rough estimate of the selection fraction is 22%. Sources with dominant contributions from stellar emission, though they may comprise a large fraction of the total AGN population, will be excluded from this survey. However, the power-law technique is intended to reliably select active sources with little contamination, and in particular can select heavily obscured AGNs (and hence AGNs missed by X-ray, visible, or radio surveys). Thus, it provides an excellent way of supplementing other AGN selection methods and leads to a more complete AGN census for study.

We thank Mark Dickinson for supplying FIDEL data in advance of publication and Alison Coil and Christopher Willmer for advice concerning the spectroscopic data. This study has made use of data from AEGIS, a multiwavelength sky survey conducted with the Chandra, GALEX, Hubble, Spitzer, Keck, Palomar, CFHT, MMT, Subaru, VLA, and other telescopes and supported in part by the NSF and NASA. This work is based in part on observations made with the Spitzer Space Telescope, which is operated by the Jet Propulsion Laboratory, California Institute of Technology under a contract with NASA. Support for this work was provided by NASA. This work is based in part on data collected at Subaru Telescope, which is operated by the National Astronomical Observatory of Japan and on observations obtained with MegaPrime/MegaCam, a joint project of CFHT and CEA/DAPNIA, at the Canada-France-Hawaii Telescope (CFHT) which is operated by the National Research Council (NRC) of Canada, the Institut National des Sciences de l’Univers of the Centre National de la Recherche Scientifique (CNRS) of France, and the University of Hawaii. This work is based in part on data products produced at TERAPIX and the Canadian Astronomy Data Centre as part of the Canada-France-Hawaii Telescope Legacy Survey, a collaborative project of NRC and CNRS. The observations reported here were obtained in part at the MMT Observatory, a facility operated jointly by the Smithsonian Institution and the University of Arizona. PB acknowledges research support from the Natural Sciences and Engineering Research Council of Canada.

Facilities: CFHT, CXO, Keck:II, Spitzer (IRAC, MIPS), Subaru (Suprime), VLA, MMT (Megacam, Hectospec)

REFERENCES

- Assef, R. J., et al. 2010, *ApJ*, 713, 970
- Alexander, D. M., Brandt, W. N., Hornschemeier, A. E., Garmire, G. P., Schneider, D. P., Bauer, F. E., & Griffiths, R. E. 2001, *AJ*, 122, 2156
- Alonso-Herrero, A., et al. 2006, *ApJ*, 640, 167
- Antonucci, R. 1993, *ARA&A*, 31, 473
- Appleton, P. N., et al. 2004, *ApJS*, 154, 147
- Barger, A. J., Cowie, L. L., Brandt, W. N., Capak, P., Garmire, G. P., Hornschemeier, A. E., Steffen, A. T., & Wehner, E. H. 2002, *AJ*, 124, 1839
- Barger, A. J., Cowie, L. L., Capak, P., Alexander, D. M., Bauer, F. E., Fernandez, E., Brandt, W. N., Garmire, G. P., & Hornschemeier, A. E. 2003, *AJ*, 126, 632

- Barmby, P., et al. 2006, *ApJ*, 642, 126
- Barmby, P., Huang, J.-S., Ashby, M. L. N., Eisenhardt, P. R. M., Fazio, G. G., Willner, S. P., & Wright, E. L. 2008, *ApJS*, 177, 431
- Barvainis, R. 1987, *ApJ*, 320, 537
- Bauer, F. E., Alexander, D. M., Brandt, W. N., Schneider, D. P., Treister, E., Hornschemeier, A. E., & Garmire, G. P. 2004, *AJ*, 128, 2048
- Brand, K., et al. 2006, *ApJ*, 644, 143
- Brinkmann, W., Laurent-Muehleisen, S. A., Voges, W., Siebert, J., Becker, R. H., Brotherton, M. S., White, R. L., & Gregg, M. D. 2000, *A&A*, 356, 445
- Bundy, K., et al. 2006, *ApJ*, 651, 120
- Cardamone, C. N., et al. 2008, *ApJ*, 680, 130
- Carleton, N. P., Elvis, M., Fabbiano, G., Willner, S. P., Lawrence, A., & Ward, M. 1987, *ApJ*, 318, 595
- Civano, F., Comastri, A., & Brusa, M. 2005, *MNRAS*, 358, 693
- Coil, A. L., Newman, J. A., Kaiser, N., Davis, M., Ma, C.-P., Kocevski, D. D., & Koo, D. C. 2004, *ApJ*, 617, 765
- Coil, A. L., et al. 2009, *ApJ*, 701, 1484
- Coleman, G. D., Wu, C.-C., & Weedman, D. W. 1980, *ApJS*, 43, 393
- Comastri, A., Fiore, F., Vignali, C., Matt, G., Perola, G. C., & La Franca, F. 2001, *MNRAS*, 327, 781
- Condon, J. J. 1992, *ARA&A*, 30, 575
- Daddi, E., et al. 2007, *ApJ*, 670, 173
- Dale, D. A., et al. 2005, *ApJ*, 633, 857
- Dale, D. A., et al. 2007, *ApJ*, 655, 863
- Davis, M., et al. 2003, in *Society of Photo-Optical Instrumentation Engineers (SPIE) Conf. Ser.*, ed. P. Guhathakurta, 4834, 161

- Davis, M., et al. 2007, ApJ, 660, L1
- Dey, A., et al. 2008, ApJ, 677, 943
- Donley, J. L., Rieke, G. H., Perez-Gonzalez, P. G., & Barro, G. 2008, ApJ, 687, 111
- Donley, J. L., Rieke, G. H., Pérez-González, P. G., Rigby, J. R., & Alonso-Herrero, A. 2007, ApJ, 660, 167
- Donley, J. L., Rieke, G. H., Rigby, J. R., & Pérez-González, P. G. 2005, ApJ, 634, 169
- Elvis, M., Wilkes, B. J., McDowell, J. C., Green, R. F., Bechtold, J., Willner, S. P., Oey, M. S., Polonski, E., & Cutri, R. 1994, ApJS, 95, 1
- Fazio, G. G., et al. 2004, ApJS, 154, 10
- Fiore, F., et al. 2008, ApJ, 672, 94
- Fiore, F., et al. 2009, ApJ, 693, 447
- Georgakakis, A., et al. 2008, MNRAS, 385, 2049
- Georgantopoulos, I., Georgakakis, A., & Akylas, A. 2007, A&A, 466, 823
- Georgantopoulos, I., Georgakakis, A., Rowan-Robinson, M., & Rovilos, E. 2008, A&A, 484, 671
- George, I. M., & Fabian, A. C. 1991, MNRAS, 249, 352
- Gilli, R., Comastri, A., & Hasinger, G. 2007, A&A, 463, 79
- Gilli, R., Salvati, M., & Hasinger, G. 2001, A&A, 366, 407
- Granato, G. L. & Danese, L. 1994, MNRAS, 268, 235
- Green, P. J., et al. 2009, ApJ, 690, 644
- Hall, P. B., et al. 2000, AJ, 120, 2220
- Harwit, M. 1981, *Cosmic Discovery*, (New York: Basic Books), Appendix A
- Hatziminaoglou, E., et al. 2005, AJ, 129, 1198
- Hickox, R. C. & Markevitch, M. 2006, ApJ, 645, 95
- Hornschemeier, A. E., et al. 2001, ApJ, 554, 742

- Huang, J.-S., et al. 2009, *ApJ*, 700, 183
- Ivezić, Ž., et al. 2002, *AJ*, 124, 2364
- Iverson, R. J., et al. 2007, *ApJ*, 660, L77
- Jiang, L., Fan, X., Ivezić, Ž., Richards, G. T., Schneider, D. P., Strauss, M. A., & Kelly, B. C. 2007, *ApJ*, 656, 680
- Klaas, U., et al. 2001, *A&A*, 379, 823
- Kotilainen, J. K., Ward, M. J., Boisson, C., Depoy, D. L., & Smith, M. G. 1992, *MNRAS*, 256, 149
- Kozłowski, S., et al. 2010, *ApJ*, 716, 530
- Lacy, M., et al. 2004, *ApJS*, 154, 166
- Laird, E. S., et al. 2009, *ApJS*, 180, 102
- Laird, E. S., Nandra, K., Hobbs, A., & Steidel, C. C. 2006, *MNRAS*, 373, 217
- La Massa, S. M., Heckman, T. M., Ptak, A., Hornschemeier, A., Martins, L., Sonnentrucker, P., & Tremonti, C. 2009, *ApJ*, 705, 568
- Lawrence, A., Ward, M., Elvis, M., Fabbiano, G., Willner, S. P., Carleton, N. P., & Longmore, A. 1985, *ApJ*, 291, 117
- Lotz, J. M., et al. 2008, *ApJ*, 672, 177
- Lutz, D., Maiolino, R., Spoon, H. W. W., & Moorwood, A. F. M. 2004, *A&A*, 418, 465
- Maccacaro, T., Gioia, I. M., Wolter, A., Zamorani, G., & Stocke, J. T. 1988, *ApJ*, 326, 680
- Matt, G., Fabian, A. C., Guainazzi, M., Iwasawa, K., Bassani, L., & Malaguti, G. 2000, *MNRAS*, 318, 173
- Maiolino, R. & Rieke, G. H. 1995, *ApJ*, 454, 95
- Martínez-Sansigre, A., Rawlings, S., Lacy, M., Fadda, D., Marleau, F. R., Simpson, C., Willott, C. J., & Jarvis, M. J. 2005, *Nature*, 436, 666
- McLeod, B., Geary, J., Ordway, M., Amato, S., Conroy, M., & Gauron, T. 2006, in *Scientific Detectors for Astronomy 2005*, *Astrophys. & Space Sci. Library*, Vol. 336, ed. J. E. Beletic, J. W. Beletic, & P. Amico, (New York: Springer), p. 337

- Mukai, K. 1993, *Legacy*, 3, 21
- Mushotzky, R. 2004, in *Supermassive Black Holes in the Distant Universe*, *Astrophys. & Space Sci. Library*, Vol. 308, ed. A. J. Barger, (Dordrecht: Kluwer), p. 53
- Mushotzky, R. F., Cowie, L. L., Barger, A. J., & Arnaud, K. A. 2000, *Nature*, 404, 459
- Nandra, K. & Pounds, K. A. 1994, *MNRAS*, 268, 405
- Narayanan, D., Hayward, C. C., Cox, T. J., Hernquist, L., Jonsson, P., Younger, J. D., & Groves, B. 2010, *MNRAS*, 401, 1613
- Nenkova, M., Ivezić, Ž., & Elitzur, M. 2002, *ApJ*, 570, L9
- Netzer, H., et al. 2007, *ApJ*, 666, 806
- Neugebauer, G., Oke, J. B., Becklin, E. E., & Matthews, K. 1979, *ApJ*, 230, 79
- Park, S. Q., et al. 2008, *ApJ*, 678, 744
- Pen, U.-L. 1999, *ApJS*, 120, 49
- Pierce, C. M., et al. 2007, *ApJ*, 660, L19
- Polletta, M., Weedman, D., Hönig, S., Lonsdale, C. J., Smith, H. E., & Houck, J. 2008, *ApJ*, 675, 960
- Pope, A., et al. 2008, *ApJ*, 689, 127
- Rafter, S. E., Crenshaw, D. M., & Wiita, P. J. 2009, *AJ*, 137, 42
- Ramos Almeida, C., Rodríguez Espinosa, J. M., Barro, G., Gallego, J., & Pérez-González, P. G. 2009, *AJ*, 137, 179
- Rees, M. J., Silk, J., Warner, M. W., & Wickramasinghe, N. C. 1969, *Nature*, 223, 788
- Rieke, G. H. & Lebofsky, M. J. 1981, *ApJ*, 250, 87
- Rieke, G. H. & Low, F. J. 1975, *ApJ*, 199, L13
- Rieke, G. H., et al. 2004, *ApJS*, 154, 25
- Rieke, G. H., Alonso-Herrero, A., Weiner, B. J., Pérez-González, P. G., Blaylock, M., Donley, J. L., & Marcillac, D. 2009, *ApJ*, 692, 556

- Rigby, J. R., Rieke, G. H., Pérez-González, P. G., Donley, J. L., Alonso-Herrero, A., Huang, J.-S., Barmby, P., & Fazio, G. G. 2005, *ApJ*, 627, 134
- Roche, P. F., Aitken, D. K., Smith, C. H., & Ward, M. J. 1991, *MNRAS*, 248, 606
- Salim, S., et al. 2009, *ApJ*, 700, 161
- Silverman, J. D., et al. 2008, *ApJ*, 679, 118
- Simpson, C., et al. 2006, *MNRAS*, 372, 741
- Steidel, C. C., Hunt, M. P., Shapley, A. E., Adelberger, K. L., Pettini, M., Dickinson, M., & Giavalisco, M. 2002, *ApJ*, 576, 653
- Stern, D., et al. S. P. 2005, *ApJ*, 631, 163
- Stickel, M., Rieke, G. H., Kuehr, H., & Rieke, M. J. 1996, *ApJ*, 468, 556
- Szokoly, G. P., et al. 2004, *ApJS*, 155, 271
- Tozzi, P., et al. 2006, *A&A*, 451, 457
- Ueda, Y., Akiyama, M., Ohta, K., & Miyaji, T. 2003, *ApJ*, 598, 886
- Urry, C. M., & Padovani, P. 1995, *PASP*, 107, 803
- Ward, M. J., Geballe, T., Smith, M., Wade, R., & Williams, P. 1987, *ApJ*, 316, 138
- Weedman, D. W., Le Floch, E., Higdon, S. J. U., Higdon, J. L., & Houck, J. R. 2006, *ApJ*, 638, 613
- Werner, M. W., et al. 2004, *ApJS*, 154, 1
- Worsley, M. A., Fabian, A. C., Barcons, X., Mateos, S., Hasinger, G., & Brunner, H. 2004, *MNRAS*, 352, L28
- Worsley, M. A., et al. 2005, *MNRAS*, 357, 1281
- Yun, M. S., Reddy, N. A., & Condon, J. J. 2001, *ApJ*, 554, 803

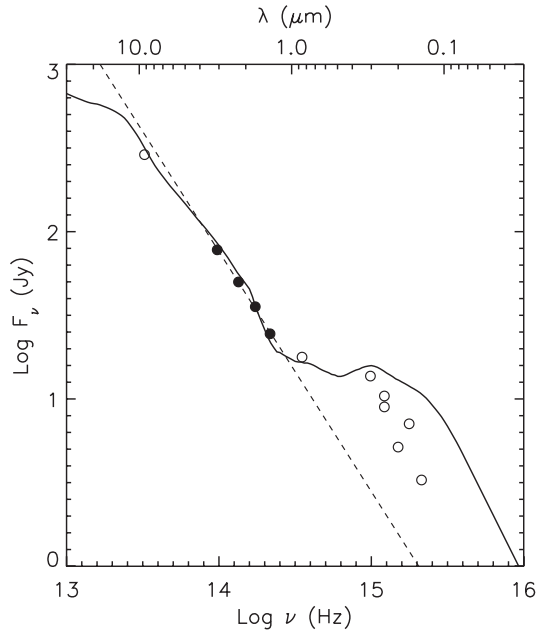


Fig. 1.— Sample SED and power-law fit for a PL AGN (EGSPL 81; see Table 2). The source was selected for having a spectroscopic $z = 1.60$, near the median redshift of the PL AGN sample. Observed flux densities (not K-corrected) are plotted from u band ($\sim 0.4 \mu\text{m}$) to $24 \mu\text{m}$ with filled symbols denoting the four IRAC bands. The wavelength scale is in the rest frame. Uncertainties in IRAC flux densities are smaller than the symbols. The dashed line represents the fitted power-law line with spectral index $\alpha_i = -1.43$. The solid line shows the median QSO SED from Elvis et al. (1994), normalized at observed $4.5 \mu\text{m}$.

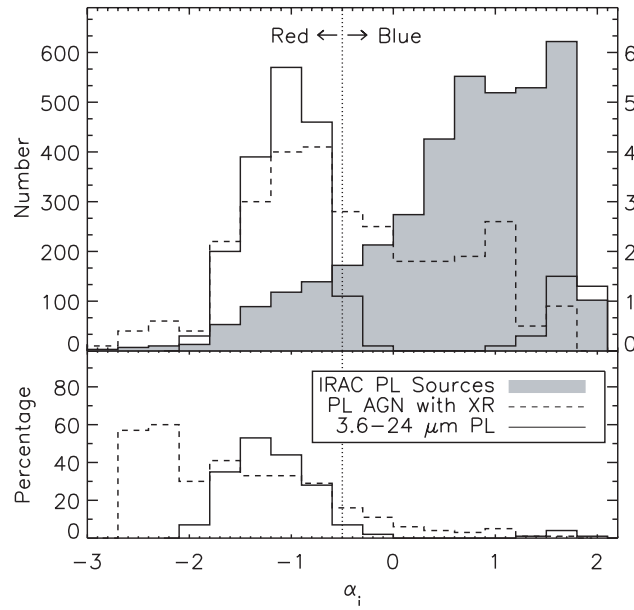


Fig. 2.— Histogram of IRAC power-law spectral indices. In the upper panel, the solid gray histogram represents all IRAC sources that are well fit by a power law (red or blue); their numbers are represented by the scale on the left. The empty dashed histogram denotes IRAC power-law sources with X-ray counterparts, and the empty solid histogram shows sources well fit to a power law from 3.6 to 24 μm . These histograms have been scaled to facilitate viewing, and their scale is on the right. Sources left of the vertical dotted line are defined here as PL AGNs. The lower panel shows the percentage of power law sources with X-ray counterparts (dashed lines) and the percentage of sources well-fit by a power law between 3.6 and 24 μm (solid lines) out of all of the red and blue IRAC power-law sources (represented by gray in the upper panel) as a function of spectral index.

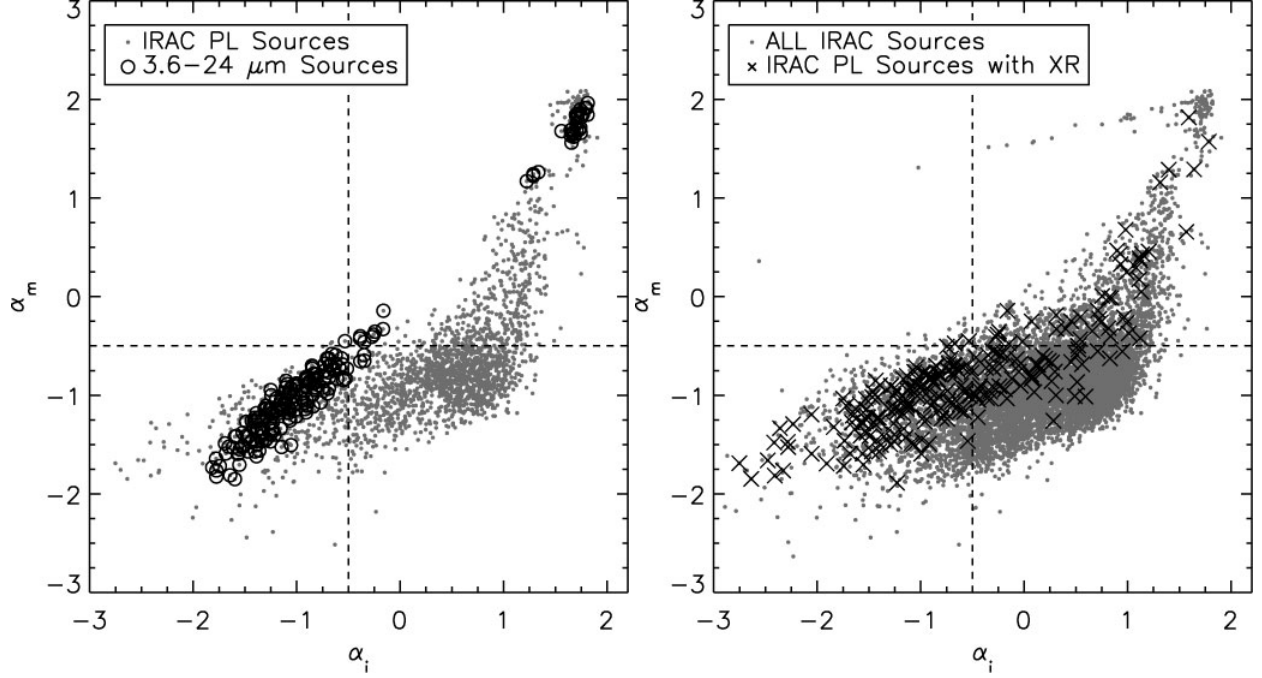


Fig. 3.— Power law spectral slopes from 3.6 to 8.0 μm (α_i) versus slopes from 3.6 to 24 μm (α_m) for sources detected by both IRAC and MIPS. Redder slopes are towards the bottom left in both panels. In the left panel, sources well fit by a power law from 3.6 to 8.0 μm are plotted as small gray dots and sources that fit a power law from 3.6 to 24 μm as large black circles. For comparison, the right panel shows the spectral indices of all sources, including those poorly fit to a power law, as small gray dots. Well-fit power-law sources with X-ray counterparts are overplotted with black X's. The dashed lines in both panels indicate the spectral slope cutoffs for our AGN sample. Objects with good fits plotted in the top right near (1.8, 2) are Galactic stars.

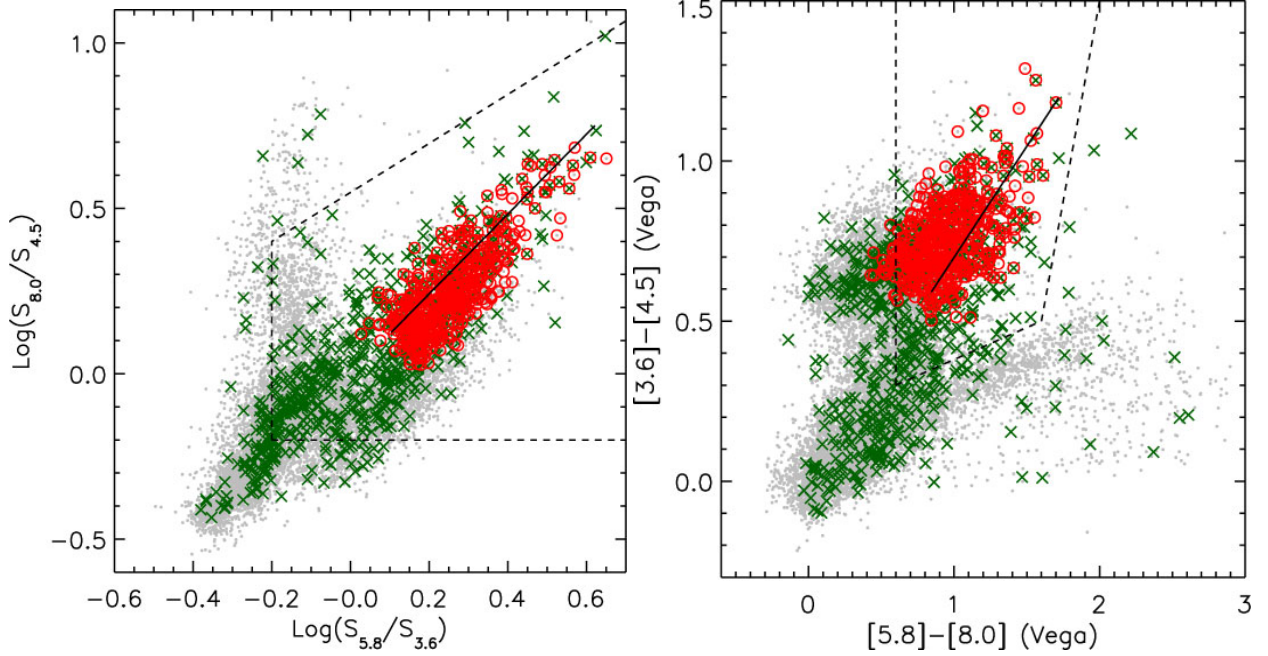


Fig. 4.— IRAC color-color diagrams. Dashed lines indicated the boundaries of the AGN selection wedges from Lacy et al. (2004) (left) and Stern et al. (2005) (right). Small gray dots represent the IRAC parent population, X-ray sources are denoted by green crosses, and the PL AGN sample is marked by red circles. The solid diagonal lines indicate where power-law sources with spectral indices from -0.5 (lower left) to -3 (upper right) would lie.

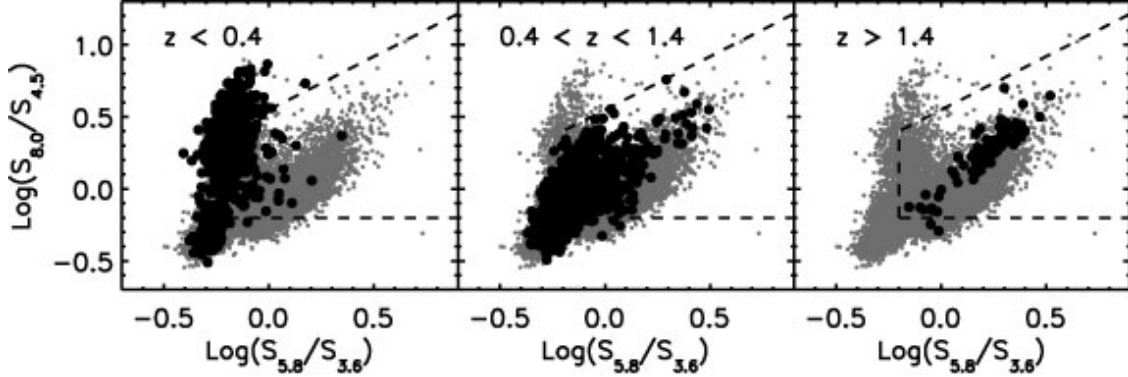


Fig. 5.— IRAC color-color plots in different redshift bins. The small gray dots represent the entire IRAC population regardless of whether they have redshift measurements, while the large black dots indicate the IRAC sources with spectroscopic redshift measurements that fall within the appropriate redshift bin. The dashed lines enclose the Lacy et al. (2004) selection wedge. The plot includes all IRAC sources with spectroscopic redshifts, not just PL AGNs.

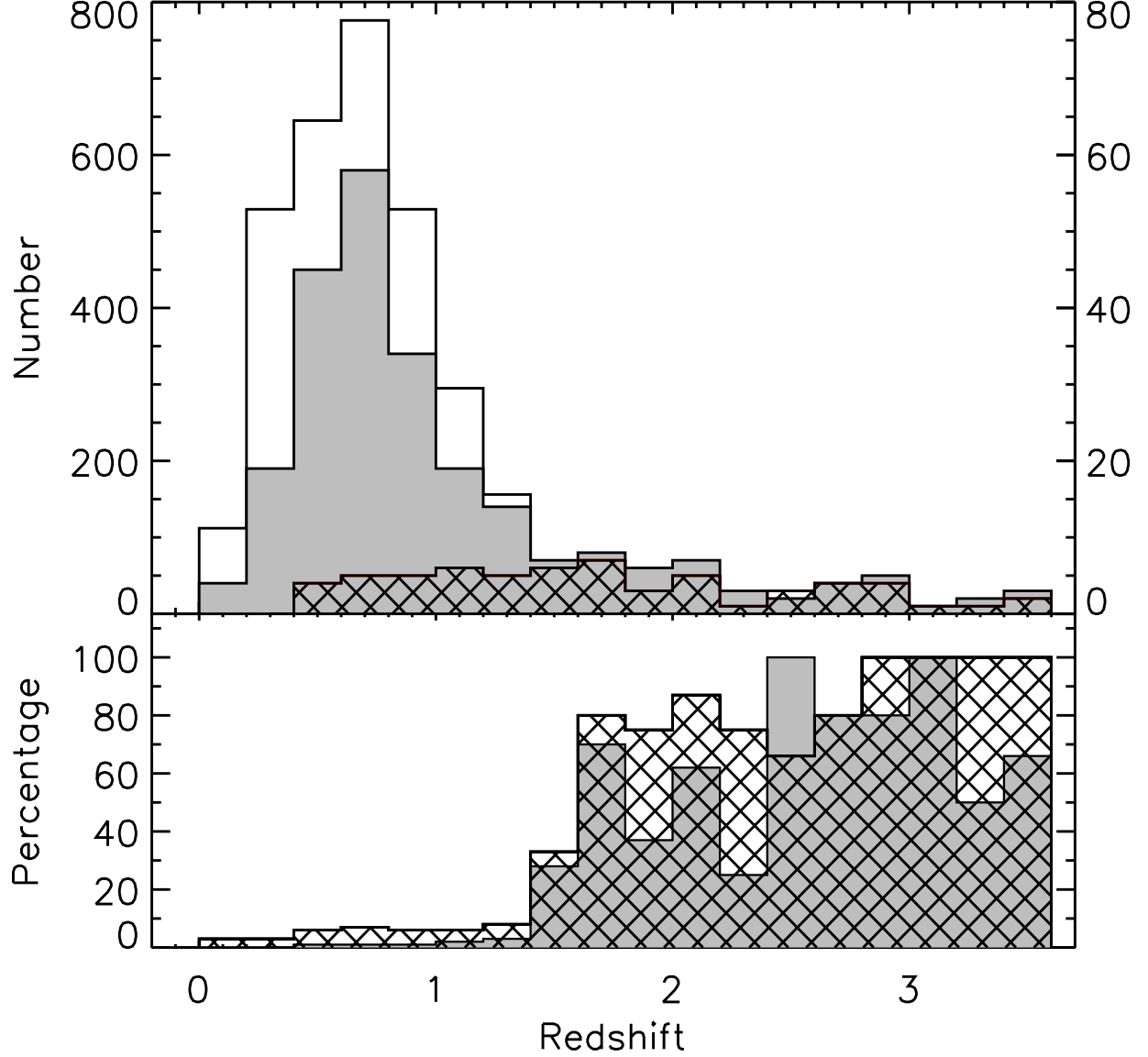


Fig. 6.— Histograms of spectroscopic redshifts. The empty histogram represents all IRAC sources with reliable redshifts (left ordinate), gray denotes sources with X-ray counterparts (right ordinate), and hatched lines denote PL AGNs (right ordinate). The bottom panel shows the percentage of X-ray (gray) and PL AGN (hatched) sources comprising the known-redshift population (empty histogram in upper panel) as a function of redshift. Nearly all IRAC sources with measured redshifts $\gtrsim 1.5$ are both X-ray sources and PL AGNs.

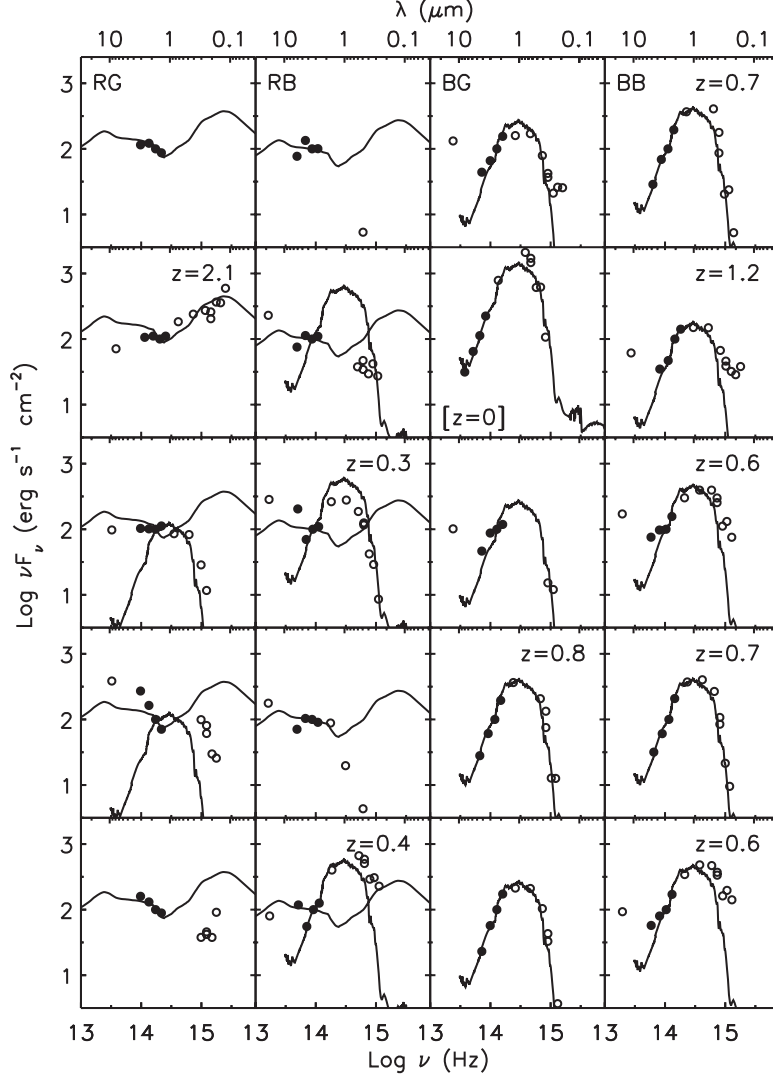


Fig. 7.— SEDs from a random subset of sources in the general IRAC population. The first column plots PL AGNs (RG = red, good fit: 4% of IRAC sample); the second column plots IRAC sources with generally red-sloping SEDs but which are poorly fit to a power law (RB = red, bad fit: 10% of sample). The third and fourth columns plot IRAC sources well fit and poorly fit respectively to a blue power law, (BG = blue, good fit: 30% of sample; BB = blue, bad fit: 55% of sample). For comparison, an elliptical template (Coleman et al. 1980) is overplotted in the last two columns and five frames of the first two, and a median QSO SED (Elvis et al. 1994) is overplotted in the first two columns. Fluxes are in arbitrary units. Data are plotted at estimated rest frame wavelengths; redshifts for individual objects are indicated where known. Otherwise, data are plotted at the median redshift for the SED type in each column: 1.6 for RG, 0.30 for RB, 0.92 for BG, and 0.70 for BB except for the second object in the BG group, for which data are plotted at $z = 0$ even though no spectroscopic redshift is available. Templates are in the rest frame and are normalized to the observed $4.5 \mu\text{m}$ flux density.

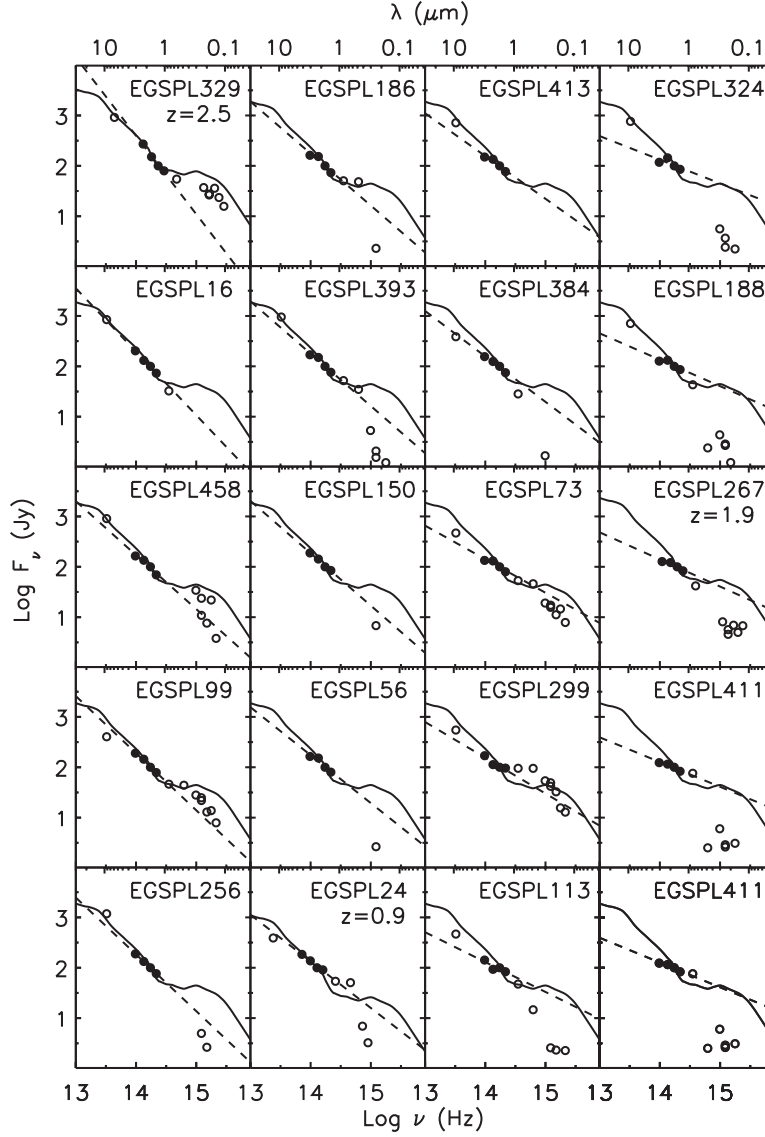


Fig. 8.— SEDs of a random subset of PL AGNs. SEDs are sorted according to spectral index, with $\alpha = -1.6$ in the top left corner and $\alpha = -0.5$ in the bottom right corner. Flux densities are plotted from u band ($0.4 \mu\text{m}$) to $24 \mu\text{m}$ with arbitrary units. (See Table 2 for actual flux densities; source identifications are indicated in the upper right of each plot.) Filled symbols represent the four IRAC bands. The dashed lines represent the best fit power law through the IRAC data points. The solid lines show the Elvis et al. (1994) median QSO template anchored at $4.5 \mu\text{m}$. The sources are plotted at rest frame if a redshift is listed below the ID. If no redshift is listed, the source does not have a reliable redshift measurement and has been shifted to the median $z = 1.6$.

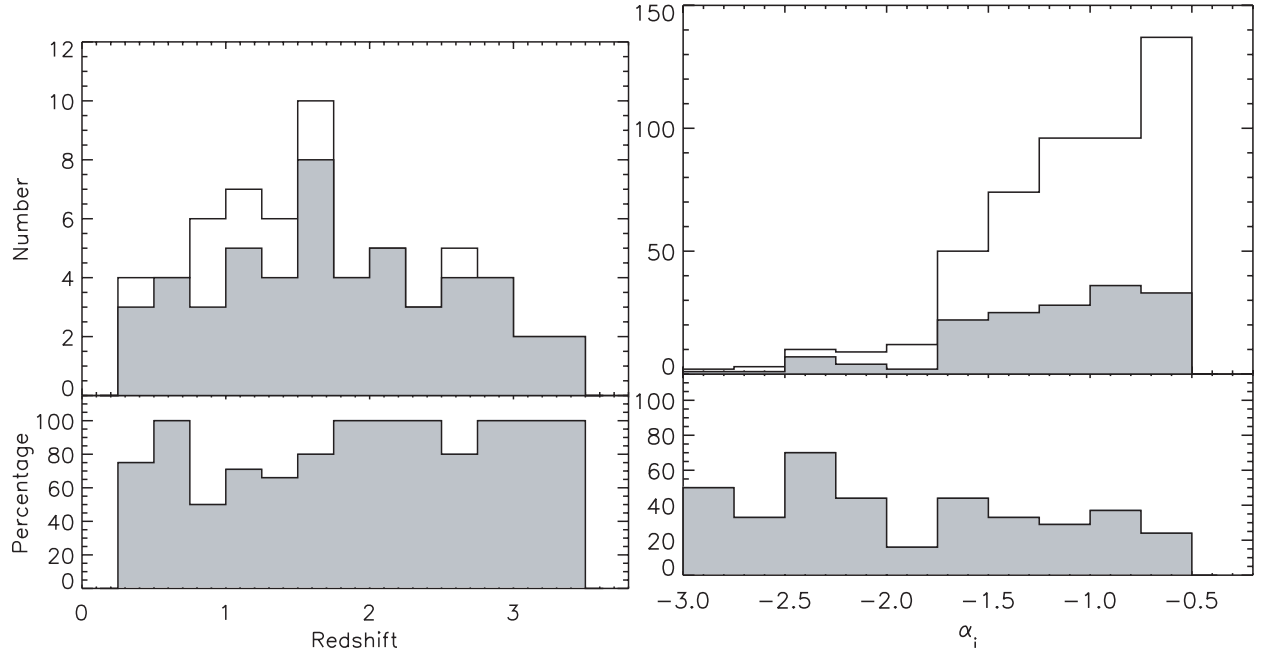


Fig. 9.— X-ray detection fractions of PL AGNs as a function of spectroscopic redshift (left) and IRAC spectral index (right). In the top panels, the empty histogram plots all PL AGNs, and the gray histograms denote PL AGNs with X-ray counterparts. The bottom panels show the X-ray detection percentages among the PL AGN sample as a function of redshift and spectral index.

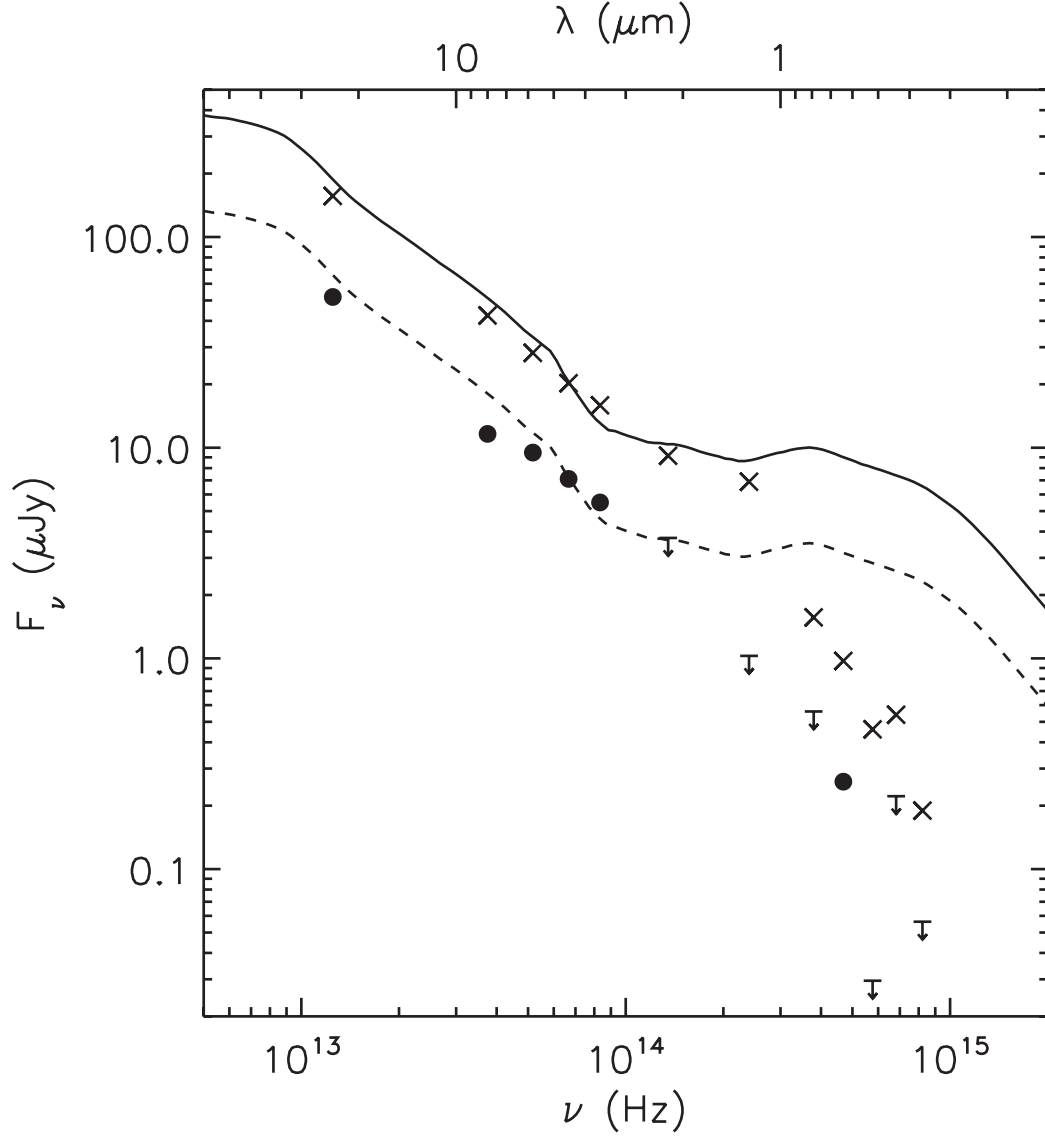


Fig. 10.— Median observed SEDs for PL AGNs with and without X-ray detections. The SEDs were constructed by taking the median observed flux density value at each band. The crosses represent PL AGNs with X-ray counterparts, and the dots and upper limits represent PL AGNs without X-ray counterpart. Upper limits are 3σ . Templates are from Elvis et al. (1994) redshifted to $z = 1.71$, the median redshift of the X-ray sample, and normalized at $4.5 \mu\text{m}$. The redshift chosen is somewhat arbitrary because only a small minority of sources have measured redshifts.

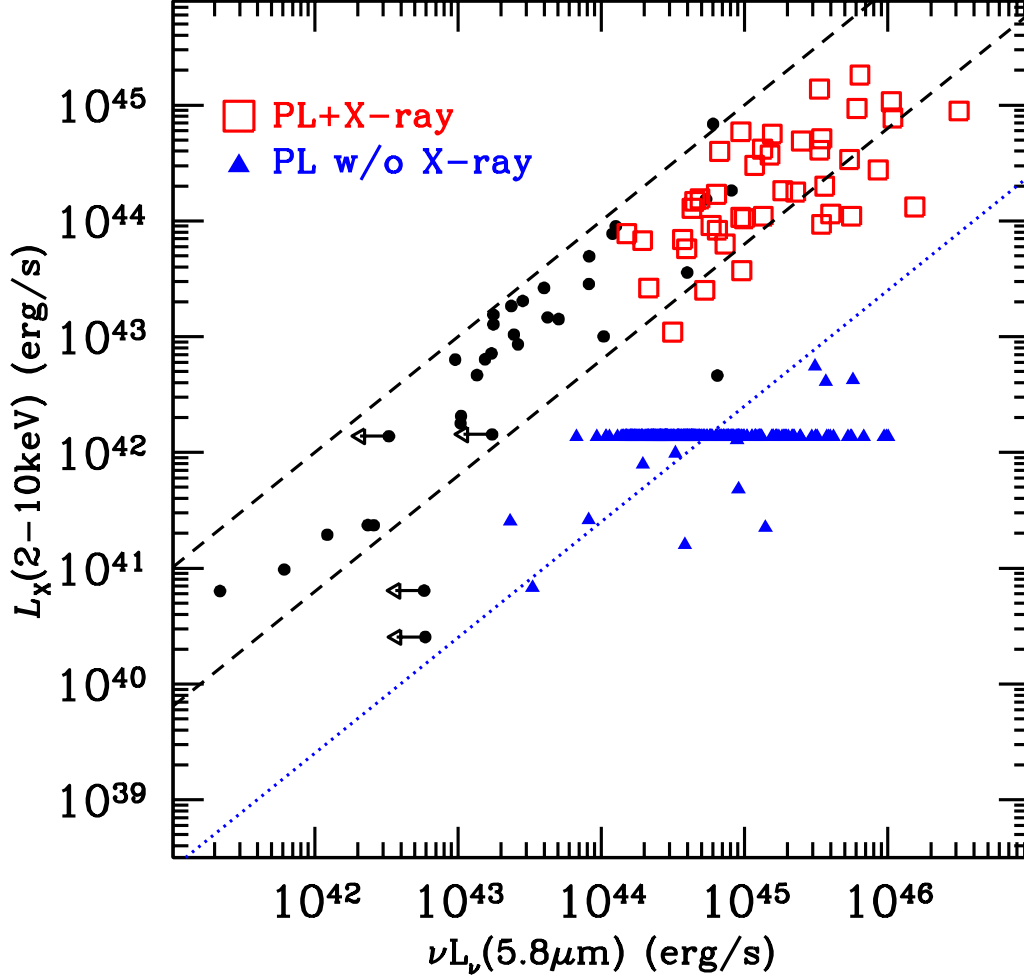


Fig. 11.— X-ray 2–10 keV luminosity plotted against rest frame 5.8 μm luminosity. Filled circles (black) denote local AGNs from the sample of Lutz et al. (2004). The dashed lines show the dispersion around the mean $L_X(2 - 10 \text{ keV})$ to $\nu L_\nu(5.8 \mu\text{m})$ relation for the Lutz et al. sample, and the blue dotted line corresponds to X-ray luminosity 100 times lower than the average for their sample. Our PL AGNs with X-ray detections and known redshifts are shown with red squares and those without X-ray detections with blue triangles. These latter sources are assigned a flux density $8.1 \times 10^{-17} \text{ erg cm}^{-2} \text{ s}^{-1}$ (the stacking signal) and $z = 1.6$ (median for the PL AGN sample) if no measured redshift. The factor of 100 is similar to the suppression of the observed X-ray emission of Compton-thick AGNs. In those sources 2–10 keV band is expected to be dominated by reflection, which is believed to represent 1-2% (Gilli et al. 2007) of the intrinsic AGN luminosity.

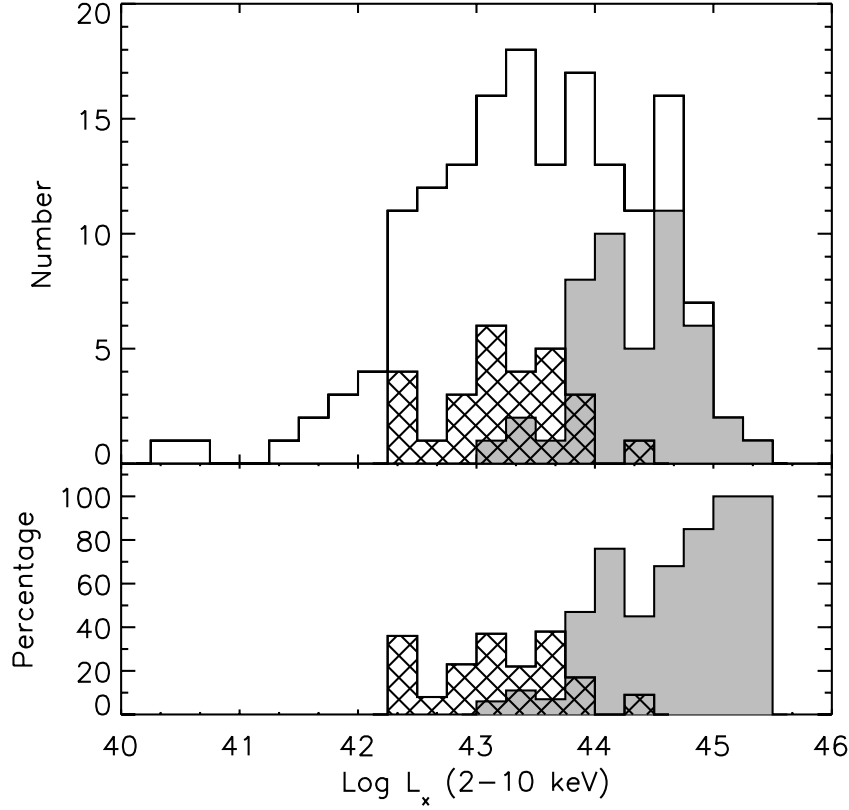


Fig. 12.— Histogram of hard band (2–10 keV) X-ray luminosities. In the top panel, the empty histogram represents all X-ray sources with reliable redshifts, the hatched histogram represents sources well fit to a blue power law in the IRAC bands, and the gray histogram represents the PL AGN sample, which make up the bulk of the high- z X-ray population. The bottom panel shows the fraction of X-ray sources detected as red (gray histogram) and blue (hatched histogram) power-law sources as a function of luminosity.

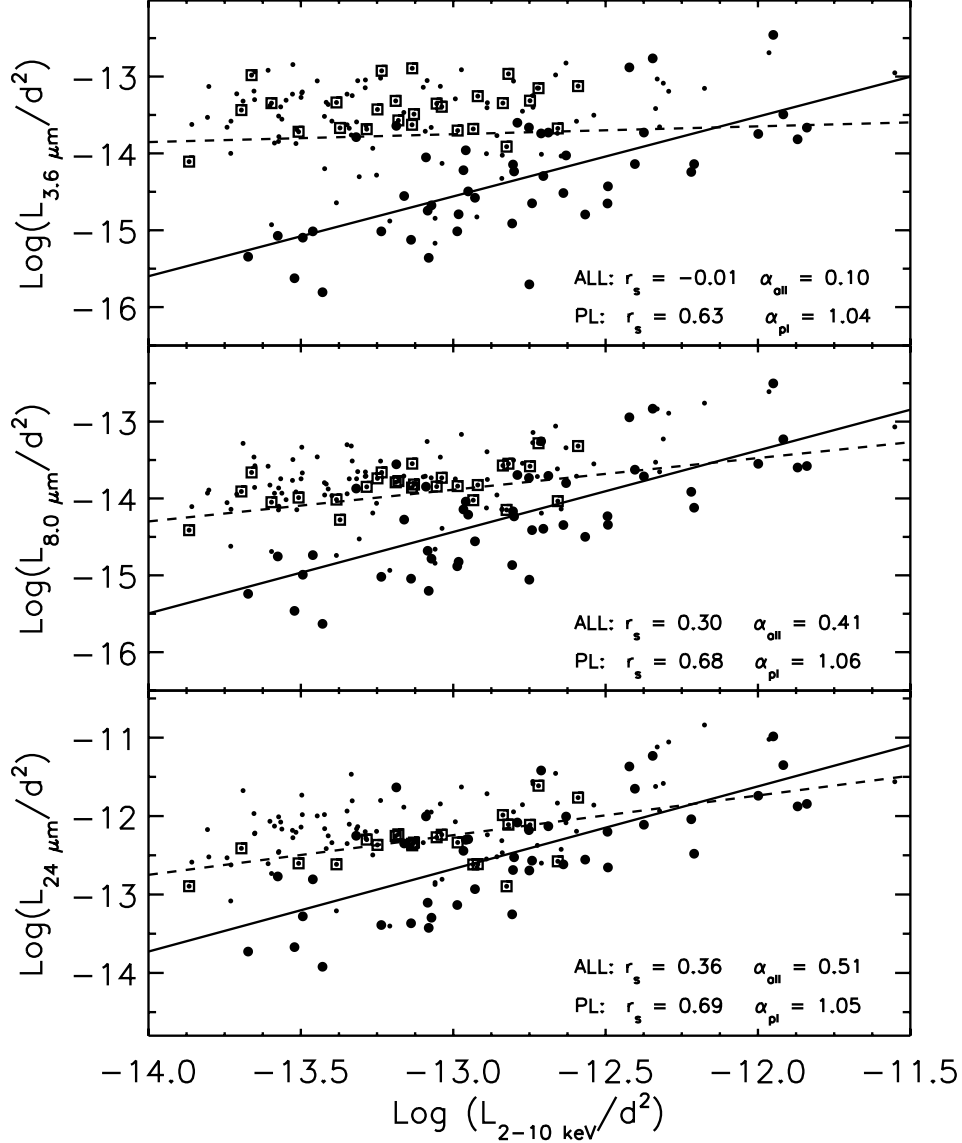


Fig. 13.— Rest frame infrared fluxes versus rest frame X-ray flux. Small dots represent all X-ray sources with infrared counterparts and known redshifts. Open squares surround X-ray sources well fit to a blue power law, and large filled circles denote the X-ray-detected PL AGNs. The solid lines indicate the best fits through the PL AGN sample, and the dashed lines denote the best fits through the parent sample. Luminosities include the respective K-corrections and have been divided by the luminosity distance squared in order to avoid non-physical correlations caused by correlation of all luminosities with distance. Units are $\text{erg s}^{-1} \text{ cm}^{-2}$. Correlation coefficients and the slopes of the best fit lines are given for the parent sample (ALL) and the red PL AGN sample (PL).

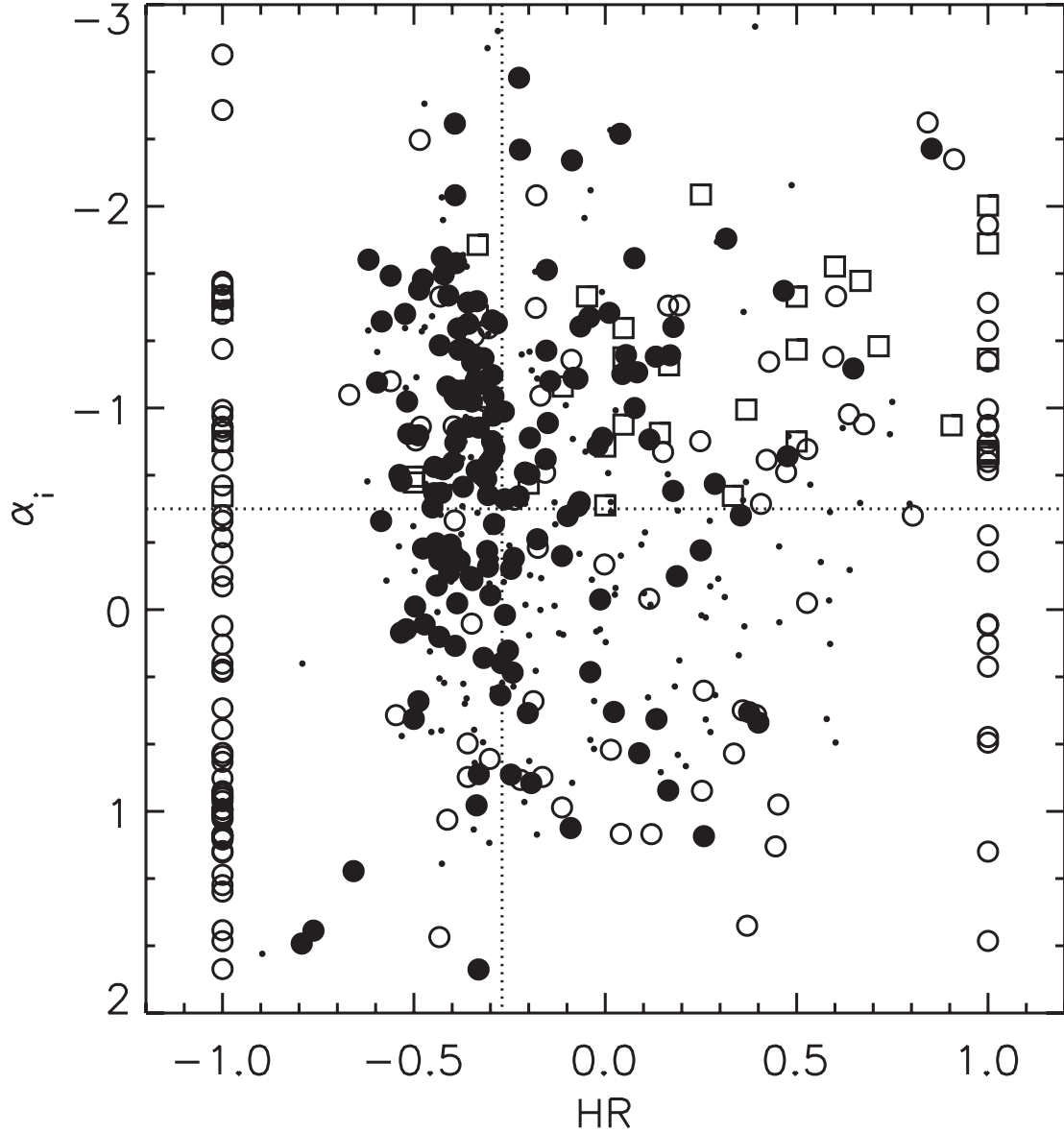


Fig. 14.— Hardness ratios for all IRAC/X-ray sources versus the 3.6 to 8.0 μm IRAC slope. Small dots represent IRAC sources with X-ray counterparts that could not be fit to a power-law; large symbols represent sources that are well fit to a power law. Filled circles indicate sources with strong hard and soft band detections (Poisson probability $< 4 \times 10^{-6}$), while open circles represent sources strongly detected in either the hard or soft band and weakly detected in the other band. (Open circles plotted at $\text{HR} < 0$ represent sources strongly detected in the soft band, and open circles at $\text{HR} > 0$ represent sources strongly detected in the hard band.) Open squares represent PL AGNs that are weakly detected (but with Poisson spurious probability $< 2 \times 10^{-2}$) in both X-ray bands. The horizontal line indicates the power-law cut-off for our selection; sources with $\alpha_i < -0.5$ (above the line) are PL AGNs. The vertical line indicates the median HR value for all of the strongly detected IRAC/X-ray sources.

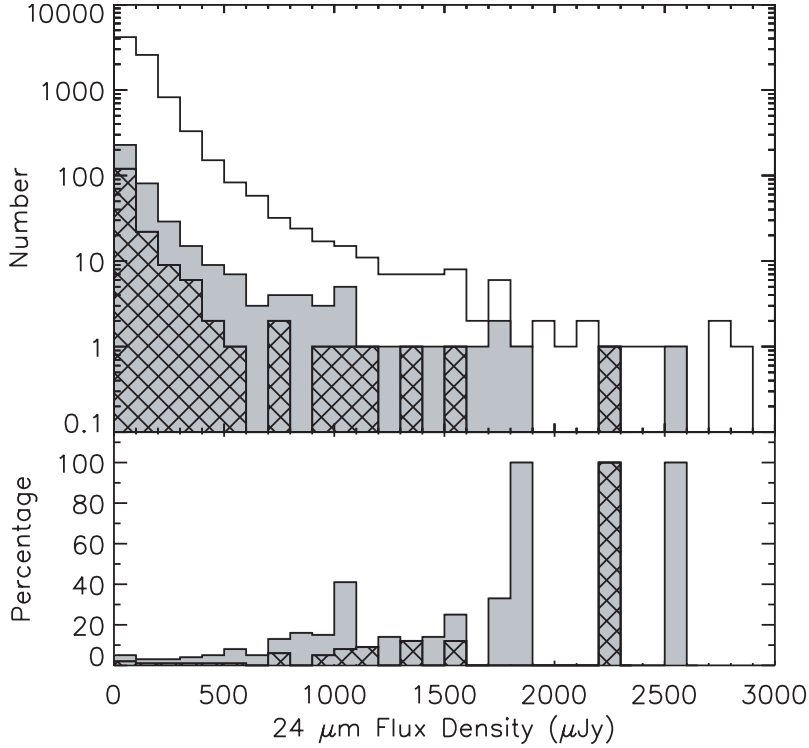


Fig. 15.— Distribution of $24\ \mu\text{m}$ flux densities. In the top panel, the empty histogram represents all IRAC sources with $24\ \mu\text{m}$ detections plotted on a logarithmic scale. The gray histogram represents sources selected as PL AGNs, and the hatched histogram represents objects with 3.6 to $24\ \mu\text{m}$ red power laws ($\alpha_m < -0.5$). The bottom panel shows the percentage of PL AGNs (gray) or 3.6 – $24\ \mu\text{m}$ red power-law sources (hatched) in the IRAC/ $24\ \mu\text{m}$ parent sample in each flux density bin.

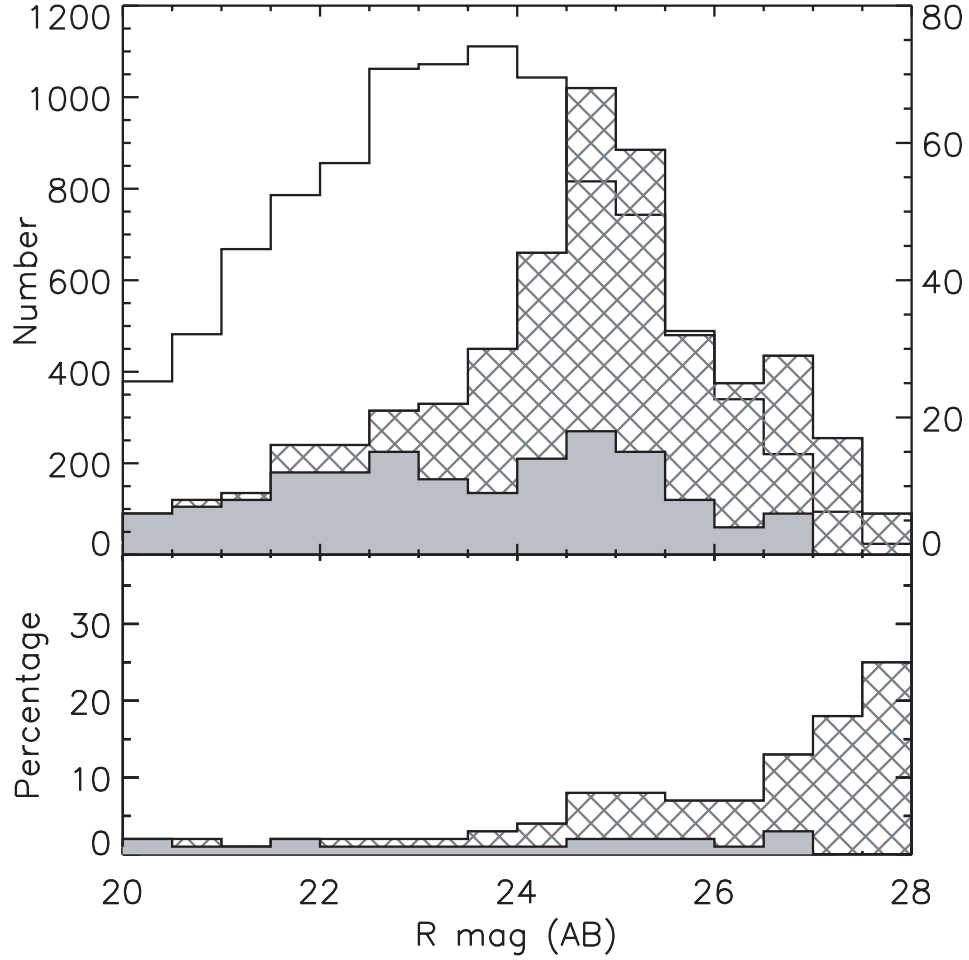


Fig. 16.— Histogram of R -band magnitudes for sources detected at R . In the top panel, the white histogram represents all IRAC sources (with 5σ detections in all IRAC bands); values are indicated by the scale on the left. The hatched histogram denotes PL AGNs, and the gray histogram denotes PL AGNs with X-ray detections, both with values indicated by the scale on the right. The bottom panel shows the percentage of PL AGNs (hatched) and the percentage of PL AGNs with X-ray detections (gray) at each R -band magnitude in the IRAC parent sample. All of the histograms exclude sources undetected at R , which are 9% of the IRAC sources and 18% of the PL AGNs.

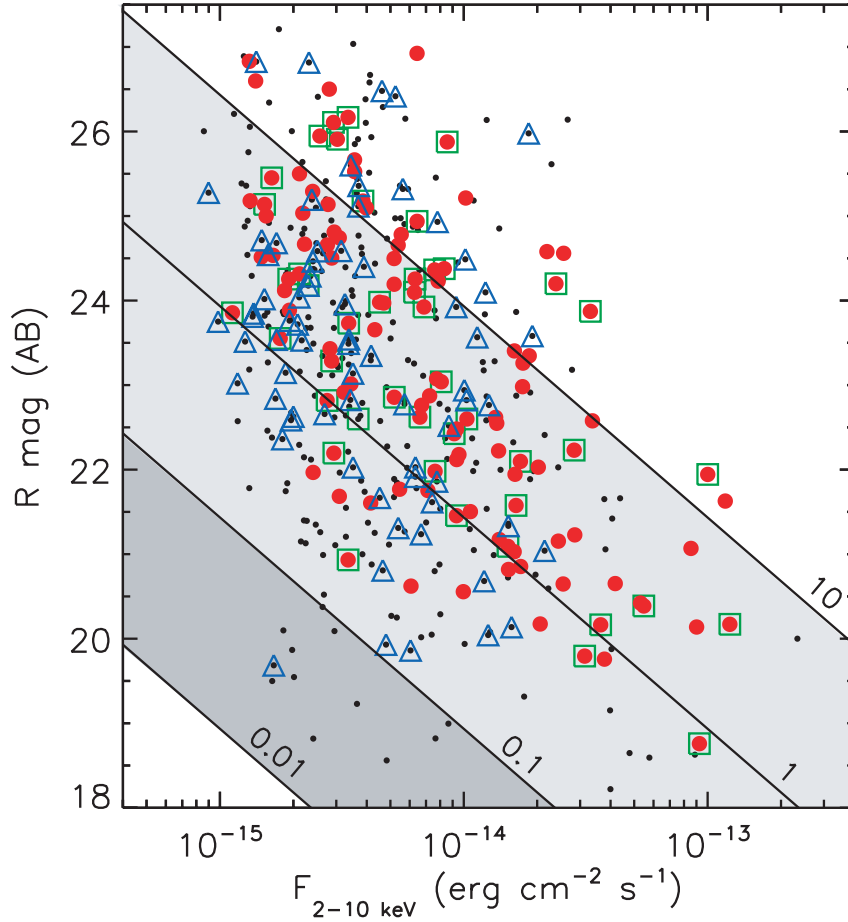


Fig. 17.— Hard X-ray flux versus R band magnitude. Small black dots indicate all IRAC sources with X-ray and R band counterparts. Large red dots represent PL AGNs, green squares represent sources that have power laws from 3.6 to 24 μm , and blue triangles indicate sources that are well fit to a blue IRAC power law. The numbers near the slanted lines indicate the X/O ratio of the line. The light shaded area denotes the region where most AGNs are expected to lie; the darker shaded area indicates the transition region that is populated by both AGNs and starbursts.

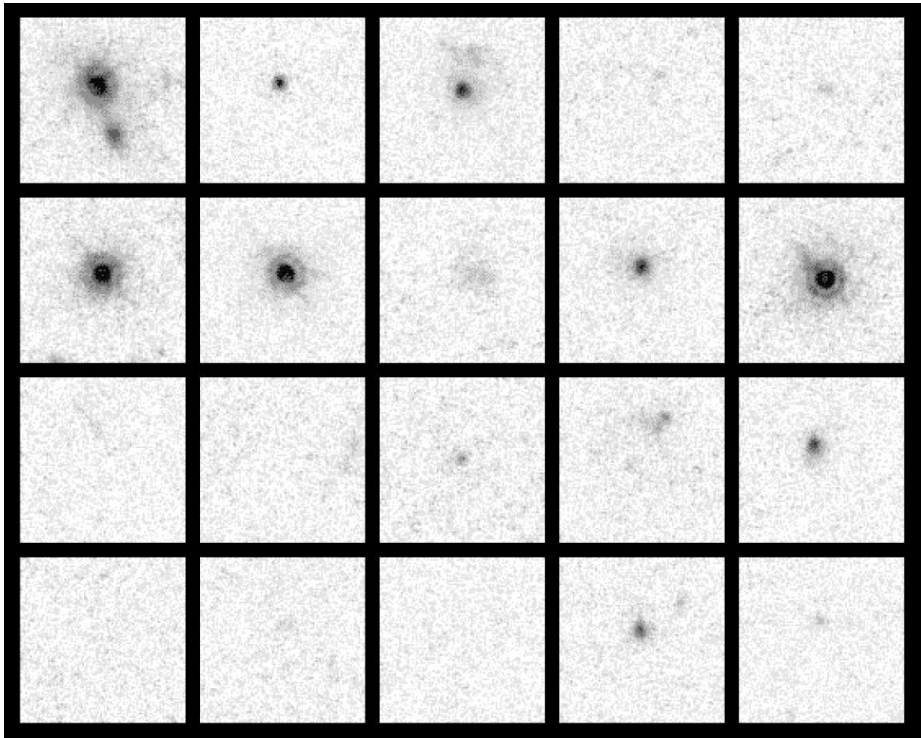


Fig. 18.— ACS I negative images for a sample of PL AGNs. The top two rows depict sources with X-ray detections, and the bottom two rows show sources without X-ray counterparts. Thumbnails are $8''$ on each side.

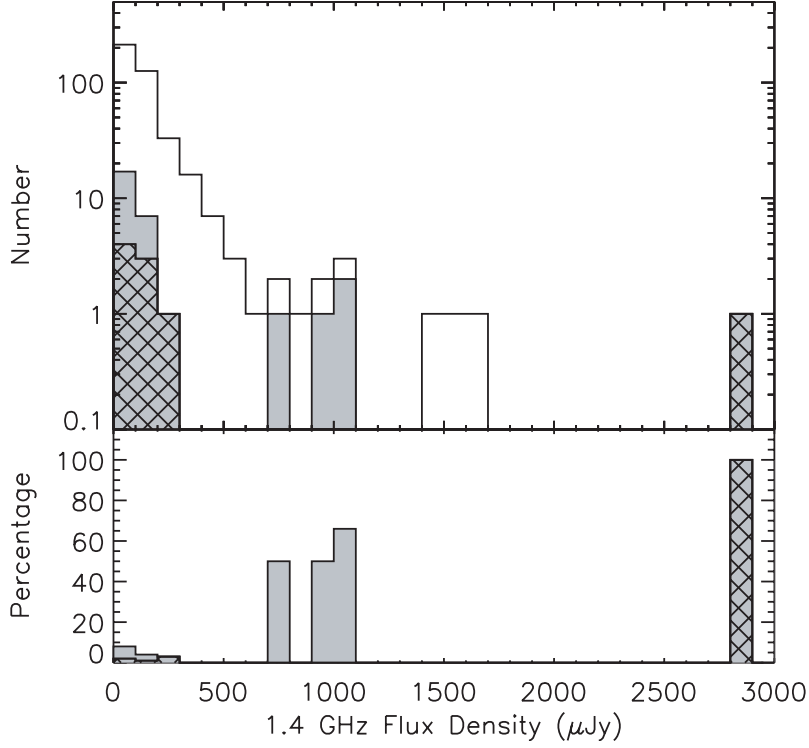


Fig. 19.— Distribution of 1.4 GHz flux densities. In the top panel, the empty histogram denotes all IRAC sources with 1.4 GHz detections. The gray histogram represents PL AGNs, and the hatched histogram shows sources that have red power laws from 3.6 to 24 μm . The bottom panel shows the percentage of radio sources at each radio flux density that are PL AGNs (gray) or have 3.6–24 μm red power law SEDs (hatched).

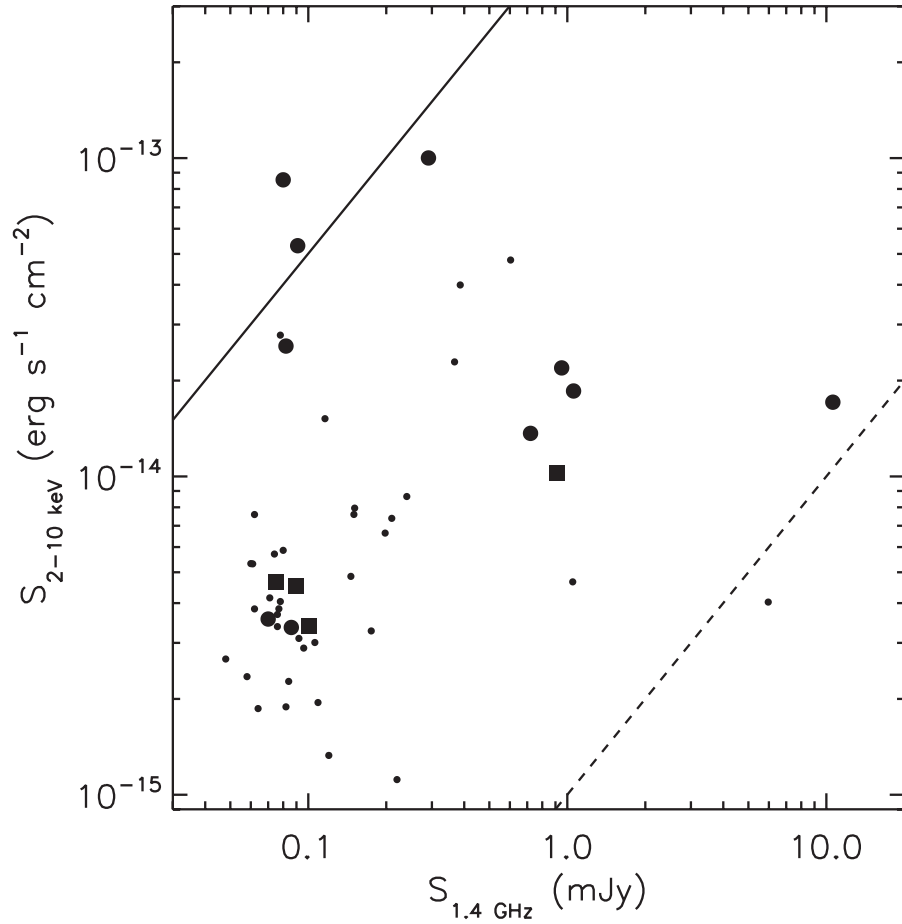


Fig. 20.— Radio flux density versus hard band X-ray flux. Small dots denote all IRAC sources with X-ray and radio detections. Filled circles represent PL AGNs, and filled squares represent objects with a blue power law from 3.6 to 8.0 μm . The solid line indicates the X-ray/radio correlation (Brinkmann et al. 2000) for radio-quiet AGNs and is given by $S_{2-10 \text{ keV}} (\text{W m}^{-2}) = 10^{-15.3} S_{1.4 \text{ GHz}} (\text{mJy})$. The dashed line indicates the correlation for starburst galaxies, with $S_{2-10 \text{ keV}} (\text{W m}^{-2}) = 10^{-18.0} S_{1.4 \text{ GHz}} (\text{mJy})$. Numerical values for both correlations come from Simpson et al. (2006, their equations 7 and 9).

Table 1. IRAC Sources and Categories of Power-Law Fits

Sample (IRAC Sources)	Fit Range	Red PL ^a	Red α ^b	Red non-PL ^c	Blue PL ^a	Blue α ^b	Blue non-PL ^c
All	3.6 – 8.0 μm	489 (4%)	–1.03	156 (10%)	3352 (30%)	0.97	6182 (55%)
With 24 μm counterparts	3.6 – 8.0 μm	399 (2%)	–1.05	1078 (14%)	1774 (22%)	1.62	4727 (59%)
With 24 μm counterparts	3.6 – 24 μm	168 (5%)	–1.11	6523 (82%)	41 (0.5%)	1.68	1247 (16%)
Red 3.6–24 μm power law ^d	3.6 – 8.0 μm	153 (91%)	–1.09	12 (7%)	3 (2%)	–0.35	0 (0%)
With X-ray counterparts	3.6 – 8.0 μm	159 (22%)	–1.09	136 (19%)	137 (19%)	0.50	287 (40%)

^aNumber and percentage of sources fit to a power law with $P_x \geq 0.1$. “All” refers to sources detected at $\geq 5\sigma$ in all four IRAC bands. ‘Red’ refers to sources with spectral index $\alpha \leq -0.5$; ‘Blue’ refers to sources with $\alpha > -0.5$.

^bMedian spectral slope

^cPercentage of red-sloping or blue-sloping sources poorly fit to a power-law

^dSources that fit a red power law in the 3.6–24 μm range

Table 2. Properties of Power-Law AGNs

EGSPL	EGSIRAC ^a	α_i^b 3.6–8	P_i^c 3.6–8 μm	α_m 3.6–24	P_m 3.6–24 μm	z	$S_{3.6}$ μJy	$S_{4.5}$ μJy	$S_{5.8}$ μJy	$S_{8.0}$ μJy	S_{24} μJy	[LNG2009]-eggs ^d	$\log L_X^e$ erg s^{-1}
1	J141427.18+520139.6	-1.12	0.29	-1.39	0.03	...	10.15	13.78	19.71	24.04	142.10
2	J141428.02+520352.8	-1.15	0.26	-1.15	0.44	...	7.11	10.35	12.84	17.78	66.16
3	J141428.13+520347.1	-1.54	0.62	-1.23	0.00	...	17.59	23.33	36.54	59.05	185.77	0008	...
4	J141431.06+520358.6	-0.62	0.21	-1.16	0.00	...	29.59	35.54	36.38	50.01	236.47	0010	...
5	J141433.18+520255.0	-2.06	0.73	-1.48	0.00	0.77	131.39	199.25	338.60	675.07	2550.26
6	J141438.02+520315.4	-1.53	0.86	-1.53	0.96	...	4.72	6.73	10.56	15.79	86.10
7	J141442.37+520241.5	-0.56	0.40	7.09	8.42	10.68	10.06	...	0023	...
8	J141443.94+520040.1	-1.39	0.65	-1.37	0.83	...	6.64	9.55	12.20	20.51	90.65
9	J141446.03+520627.7	-1.21	0.20	-1.65	0.00	...	4.71	5.69	9.81	11.72	99.86
10	J141446.13+520614.4	-0.73	0.11	-0.82	0.14	...	14.24	17.82	23.34	24.81	70.11

Note. — IRAC flux densities in this table were measured in 3'' diameter apertures and are the ones used in this paper. They are 3% higher than the final published values (Barmby et al. 2008), which should be used for future work. Table 2 is published in its entirety in the electronic edition of the Astrophysical Journal. A portion is shown here for guidance regarding its form and content.

^aIRAC IDs from the catalog published by Barmby et al. (2008).

^bCalculated IRAC power-law spectral index ($S_\nu \propto \nu^\alpha$); $\alpha \leq -0.5$ is required for selection as a PL AGN.

^cGoodness of fit expressed as a probability. The numerical value is the probability that observations of a source with a power-law SED would give the actual chi-square or larger. $P_x > 0.1$ is required for selection as a PL AGN.

^dX-ray IDs from the catalog published by Laird et al. (2009).

^eX-ray luminosity in the 2–10 keV band

Table 3: X-ray Detection Rates^a

Sample	Detection Rate	Comment	Reference
EGS PL AGNs	33%	200 ks, $P(\text{false}) < 4 \times 10^{-6}$	this paper, Laird et al. (2009)
EGS PL AGNs	40%	200 ks, $P(\text{false}) < 2 \times 10^{-2}$	this paper
EGS 3.6–24 μm PL sources	39%	200 ks, $P(\text{false}) < 4 \times 10^{-6}$	this paper, Laird et al. (2009)
All IRAC sources	6%	200 ks, $P(\text{false}) < 4 \times 10^{-6}$	this paper, Laird et al. (2009)
IRAC sources with 24 μm counterpart	7%	200 ks, $P(\text{false}) < 4 \times 10^{-6}$	this paper, Laird et al. (2009)
CDF South PL AGNs	53%	1 Ms data	Alonso-Herrero et al. (2006)
CDF North PL AGNs	55%	$P(\text{false}) < 1 \times 10^{-7}$	Donley et al. (2007)
CDF North PL AGNs	85%	$P(\text{false}) < 6 \times 10^{-3}$	Donley et al. (2007)

^aFraction of sample detected in X-rays with specified observation and detection criteria